Unusual Ni…Ni interaction in Ni(II) complexes as potential inhibitors for the development of new anti-SARS-CoV-2 Omicron drugs

Simranjeet Singh[a], and Mukesh Choudhary[a]*

---

[a] Department of Chemistry, National Institute of Technology Patna, Patna-800005 (Bihar) India.

[a.] *Corresponding author: mukesh@nitp.ac.in

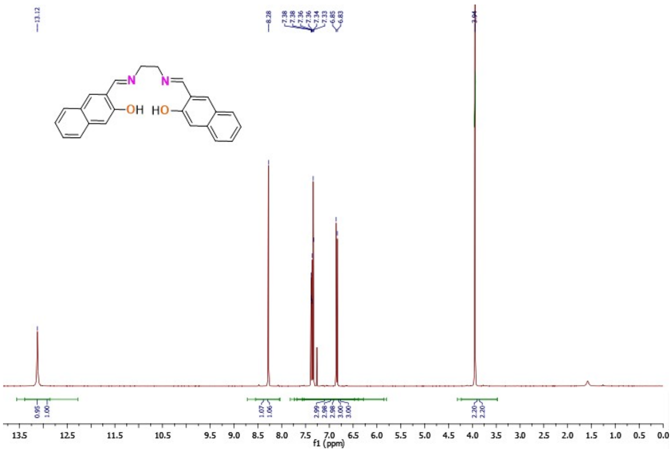

Figure S1. ^{1}H-NMR spectra of **the** salen-type N_2O_2 donor ligand (H_2L).

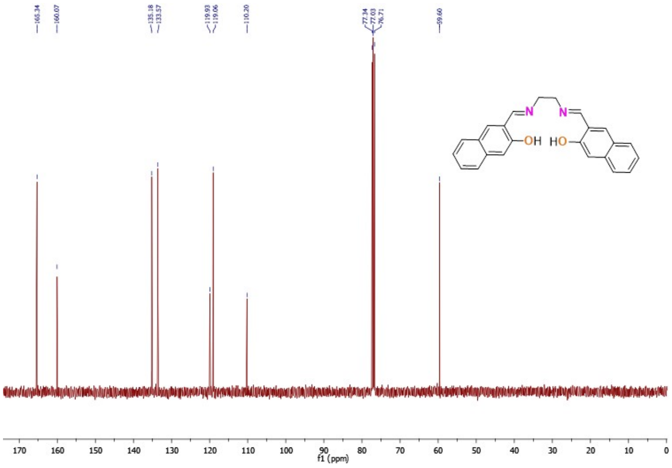

Figure S2. ^{13}C-NMR spectra of **the** salen-type N_2O_2 donor ligand (H_2L).

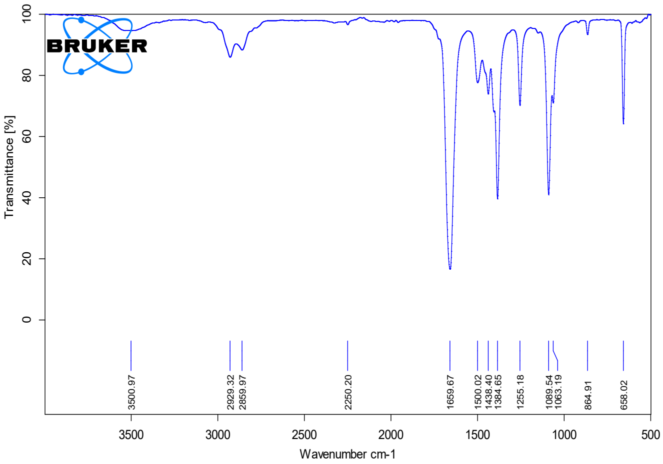

Figure S3. FT-IR spectra of **the** salen-type Schiff base ligand (H_2L).

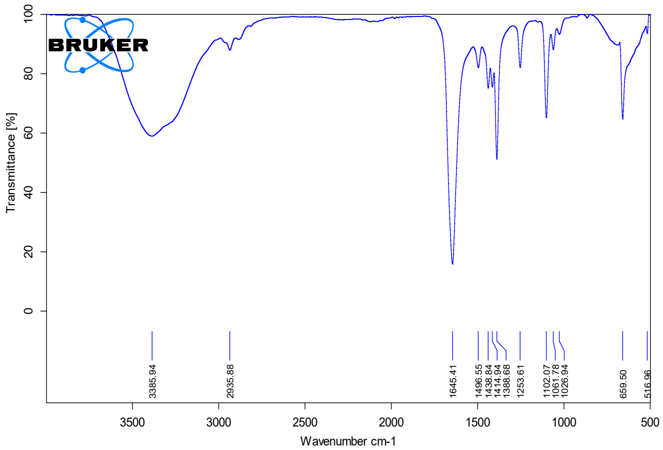

Figure S4. FT-IR spectra of **the** nickel**(II)** complex $[Ni(L)]_2$(**1**).

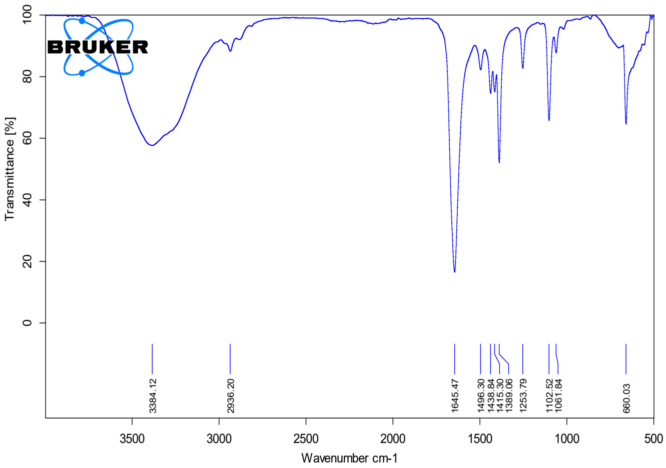

Figure S5. FT-IR spectra of **the** nickel**(II)** complex $[Ni(L)]_n$(**2**).

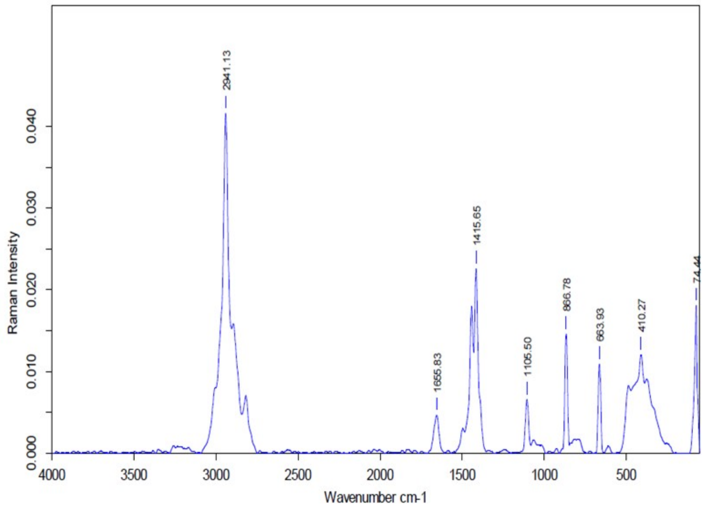

Figure S6. FT-Raman spectra of **the** nickel(**II**) complex $[Ni(L)]_2$(**1**) of salen-type Schiff base ligand (H_2L).

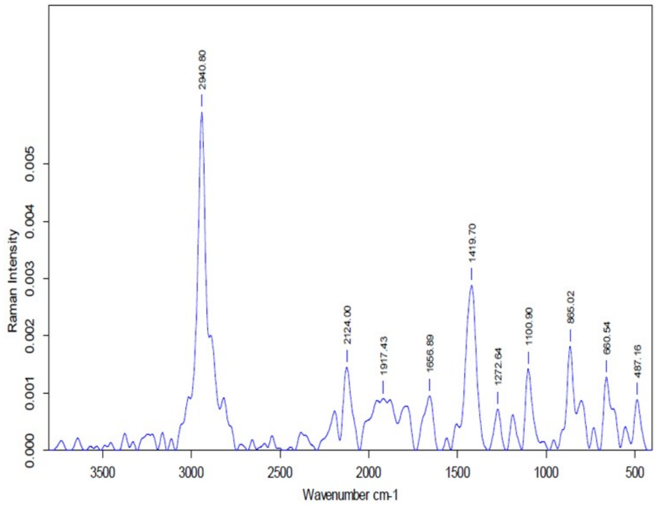

Figure S7. FT-Raman spectra of **the** nickel**(II)** complex $[Ni(L)]_n$(**2**) of salen-type Schiff base ligand (H_2L).

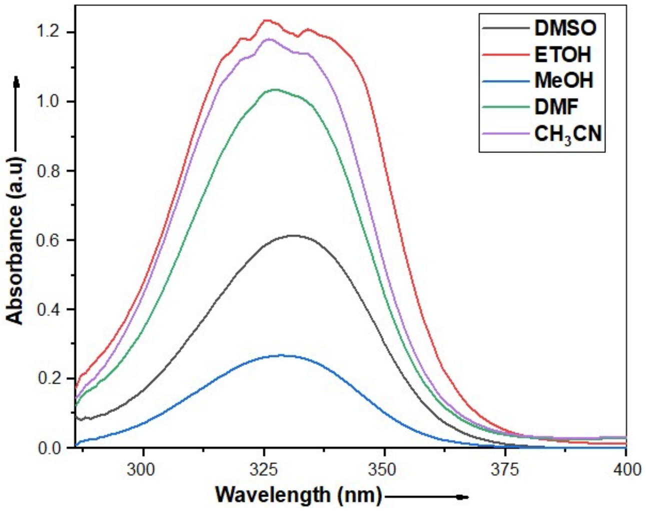

Figure S8. UV-Vis spectrum of **the** salen-type Schiff base ligand (H_2L) in different solvents at RT in 3x10^{-3} M.

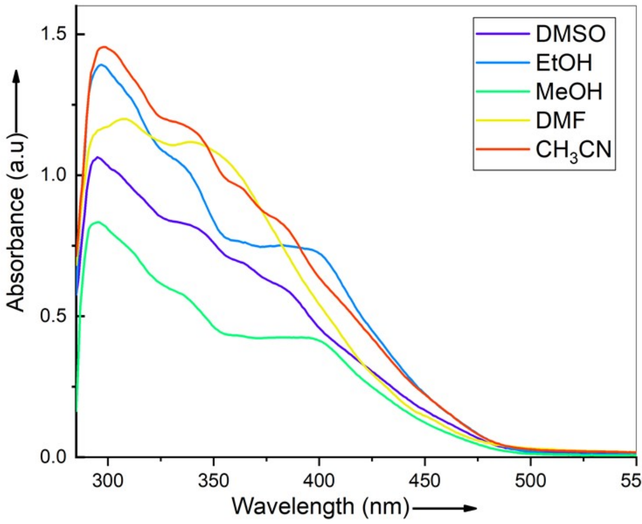

Figure S9. UV-Vis spectrum of **the** Ni(II) coordination complex $[Ni(L)]_2$(**1**) in different solvents (3x10^{-3} M) at RT.

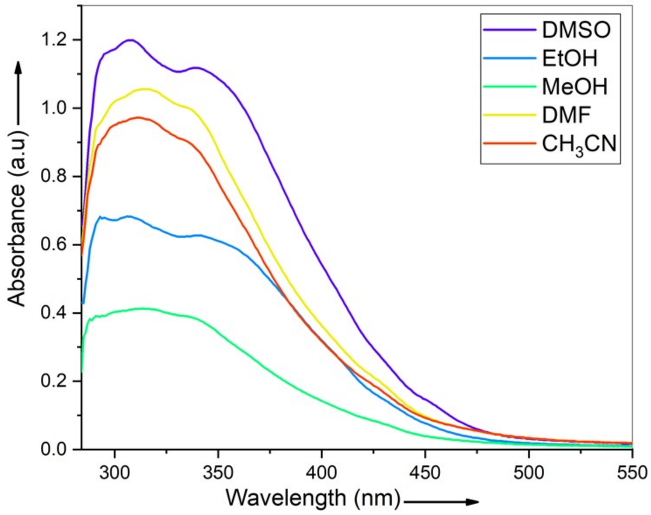

Figure S10. UV-Vis spectrum of **the** Ni(II) coordination complex $[Ni(L)]_n$(**2**) in different solvents (1x10^{-3} M) at RT.

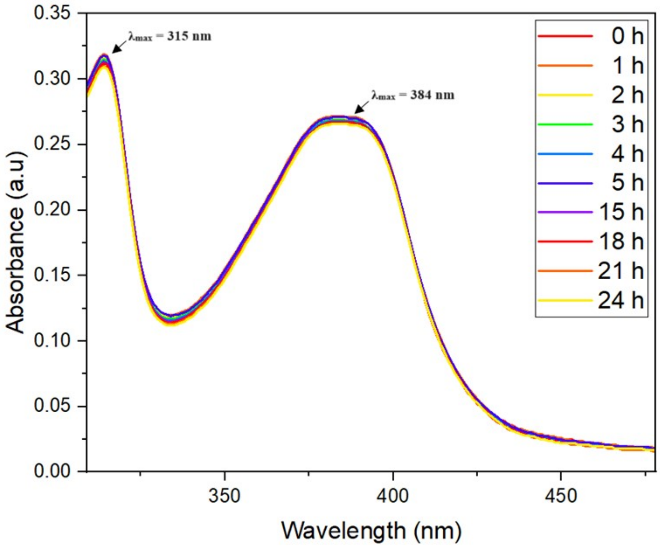

Figure S11. A representative time-dependant UV-vis spectrum of the nickel(II) coordination complex $[Ni(L)]_2$(**1**) in the aqueous solution using Milli-Q water (5μM) at regular intervals of time.

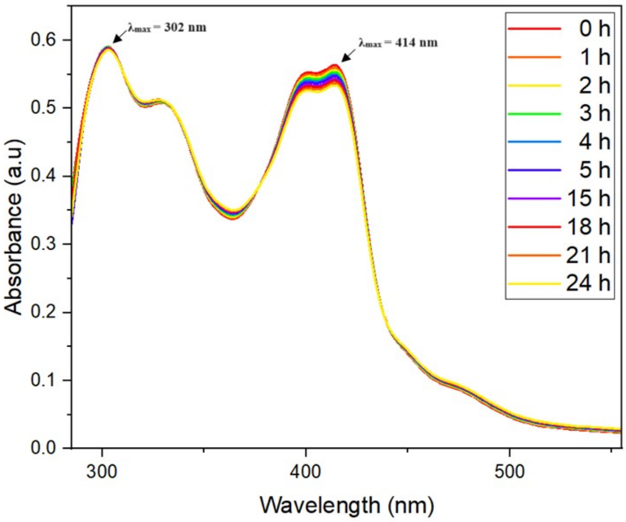

Figure S12. A representative time-dependant UV-vis spectrum of the nickel(II) coordination complex [Ni(L)]$_n$(**2**) in the aqueous solution using Milli-Q water (5μM) at regular intervals of time.

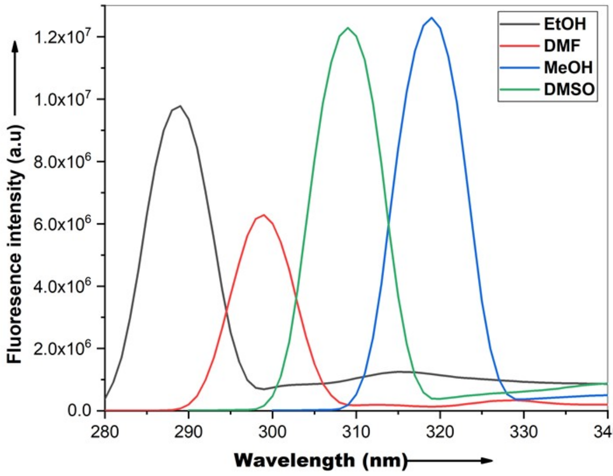

Figure S13. Fluorescence spectra of **the** salen-type Schiff base ligand (H$_2$L).

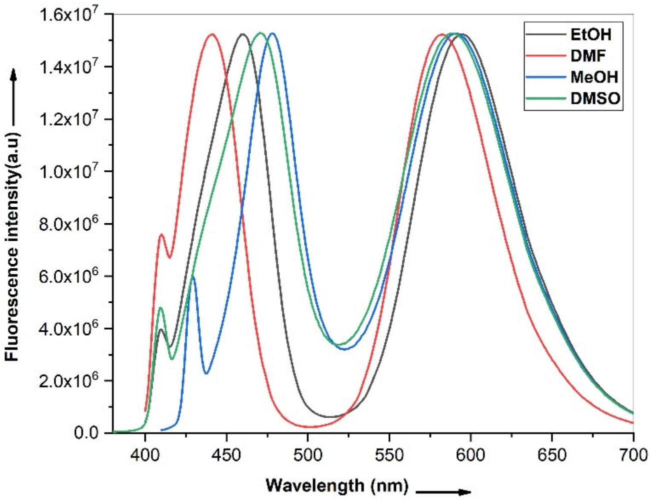

Figure S14. Fluorescence spectra of **the** Ni(II) coordination complex [Ni(L)]$_2$(**1**) of salen-type Schiff base ligand (H$_2$L).

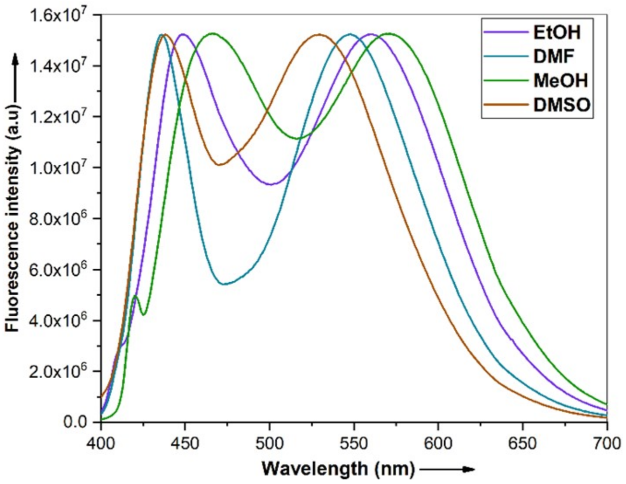

Figure S15. Fluorescence spectra of **the** Ni(II) coordination complex [Ni(L)]$_n$(**2**) of salen-type Schiff base ligand (H$_2$L).

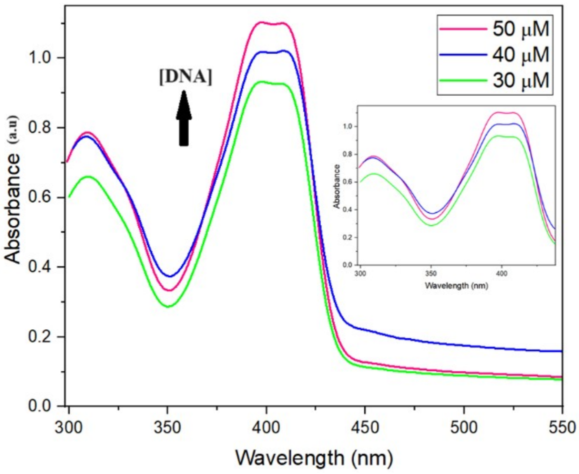

Figure S16. UV-Vis spectrum of **the** Ni(II) coordination complex [Ni(L)]$_2$(**1**) of salen-type Schiff base ligand (H$_2$L) bound to CT-DNA at different concentrations (30-50 μM).

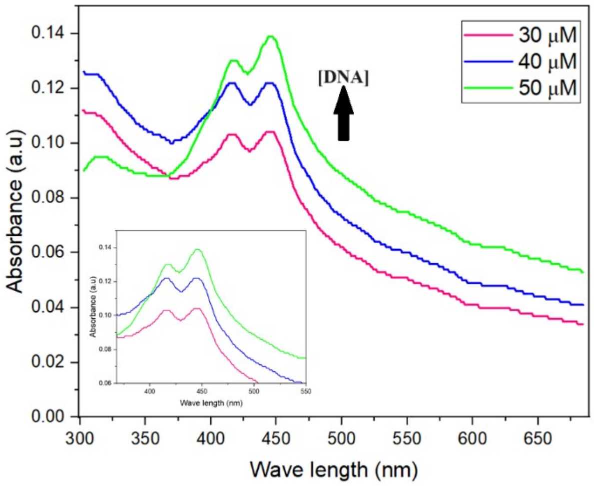

Figure S17. UV-Vis spectrum of **the** Ni(II) coordination complex [Ni(L)]$_n$(**2**) of salen-type Schiff base ligand (H$_2$L) bound to CT-DNA at different concentrations (30-50 μM).

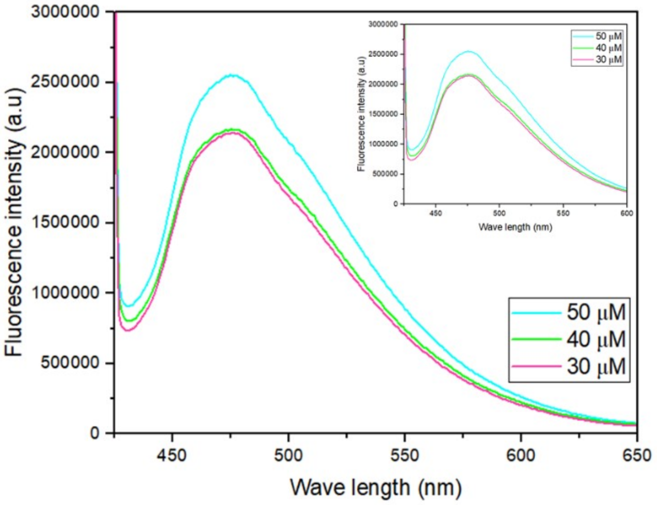

Figure S18. Fluorescence spectra of **the** Ni(II) coordination complex $[Ni(L)]_2$(**1**) of salen-type Schiff base ligand (H_2L) bound to CT-DNA at different concentrations (30-50 µM).

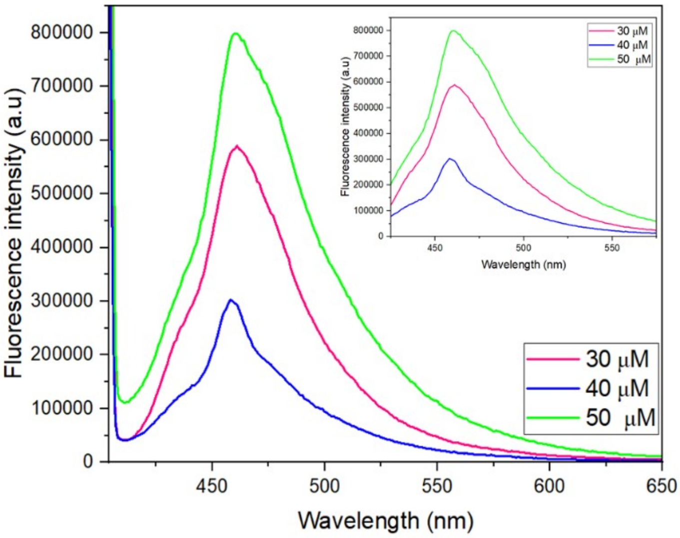

Figure S19. Fluorescence spectra of **the** Ni(II) coordination complex $[Ni(L)]_n$ (**2**) of salen-type Schiff base ligand (H_2L) bound to CT-DNA at different concentrations (30-50 µM).

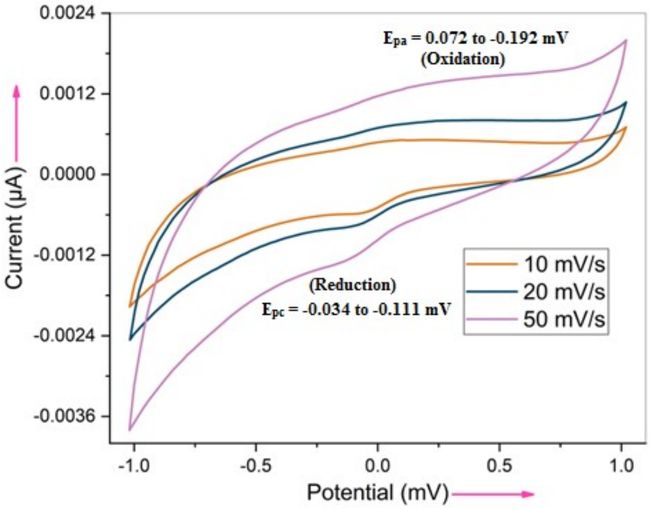

Figure S20. Cyclic voltammogram of **the** Ni(II) coordination complex $[Ni(L)]_2$(**1**) in 1M DMSO solution with TBAP as supporting electrolyte.

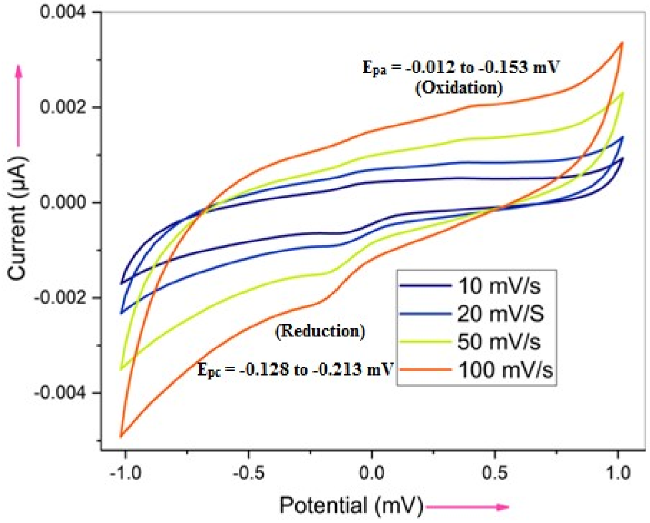

Figure S21. Cyclic voltammogram of **the** Ni(II) coordination complex $[Ni(L)]_n$(**2**) in 1M DMSO solution with TBAP as supporting electrolyte.

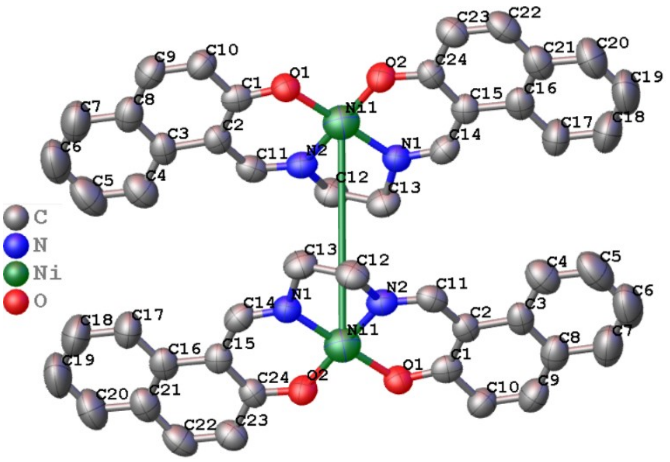

Figure S22. Molecular structure of the Ni(II) coordination complex

$[Ni(L)]_2$(**1**) with thermal ellipsoids were drawn at 50 % probability level. Hydrogen atoms are omitted for clarity.

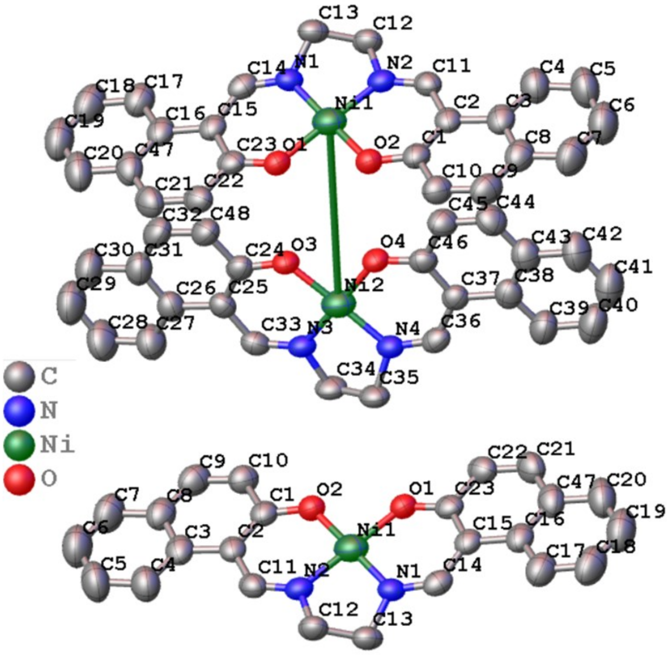

Figure S23. Molecular structure of the Ni(II) coordination complex $[Ni(L)]_n$(**2**) with thermal ellipsoids were drawn at 50 % probability level. Hydrogen atoms are omitted for clarity.

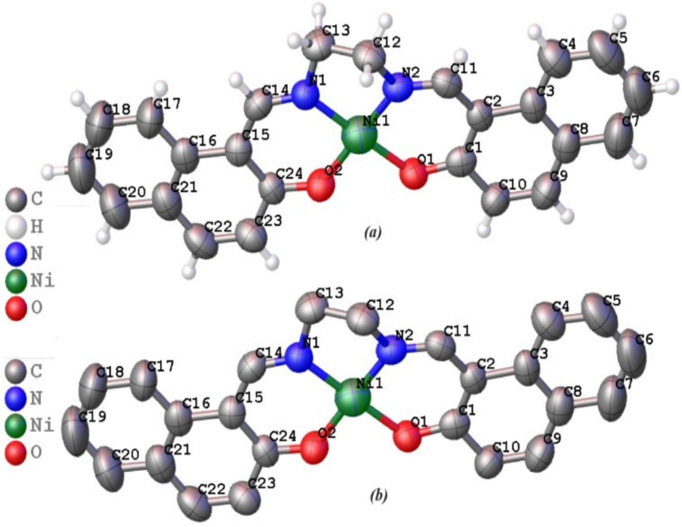

Figure S24. Asymmetrical unit representation of **the** Ni(II) coordination complex $[Ni(L)]_2$(**1**); (a) with thermal ellipsoids were drawn at 50 % probability level , and (b) Hydrogen atoms are omitted for clarity.

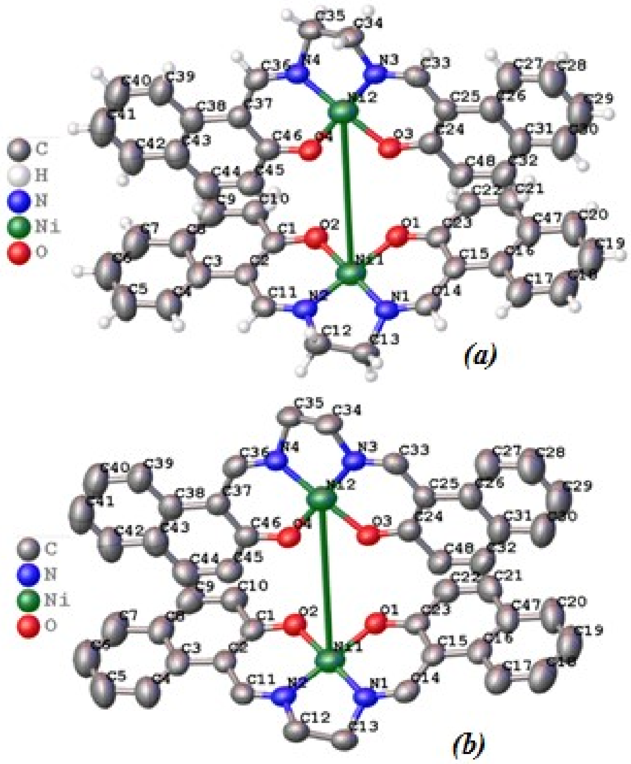

Figure S25. Asymmetrical unit representation of the Ni(II) coordination complex $[Ni(L)]_n$(**2**); (a) with thermal ellipsoids were drawn at 50 % probability level , and (b) Hydrogen atoms are omitted for clarity.

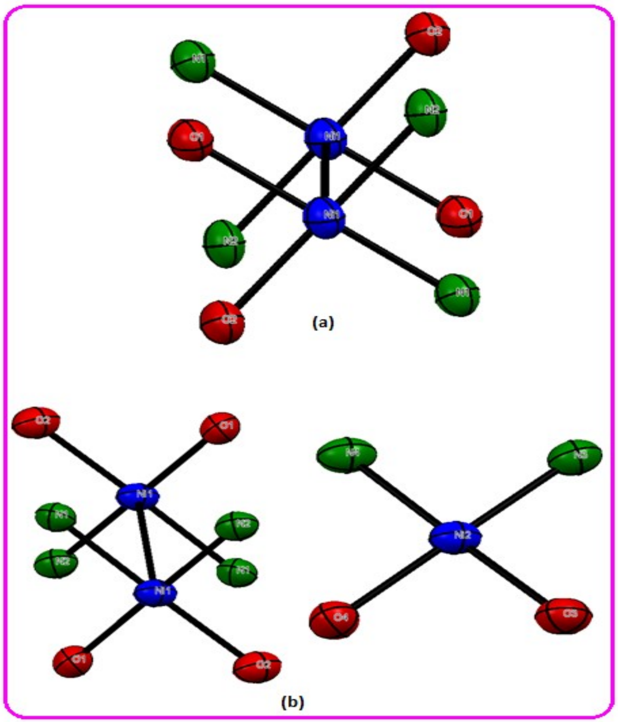

Figure S26. **(a) and (b) shows the** coordination environment of the dimer nickel centres in the Ni(II) coordination complexes $[Ni(L)]_2$(**1**) and $[Ni(L)]_n$(**2**) with selective labelling at 293(2)K.

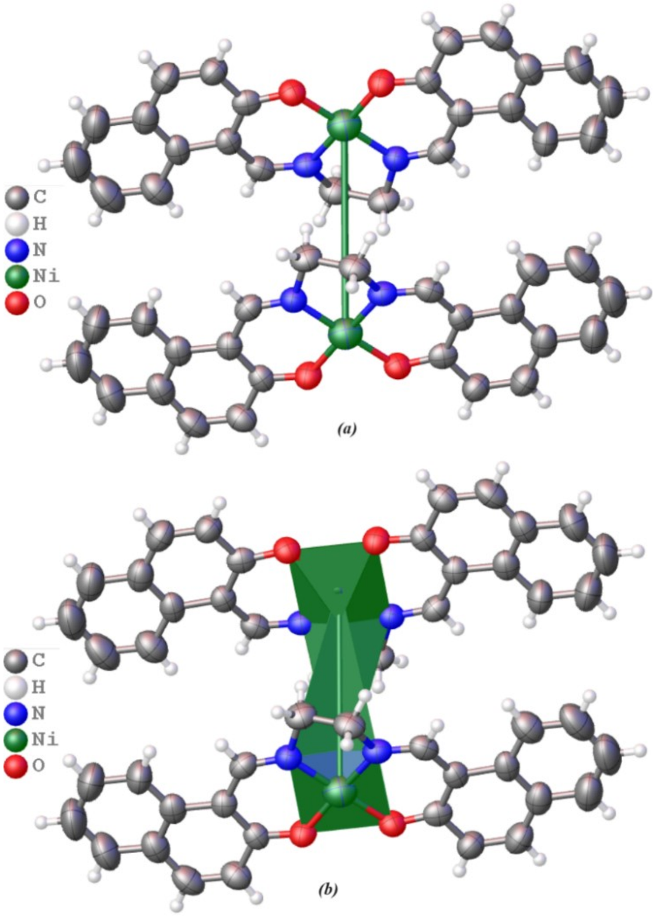

Figure S27. (a) Molecular structure and (b) polyhedron network arrangement for **the** Ni(II) coordination complex $[Ni(L)]_2$(**1**).

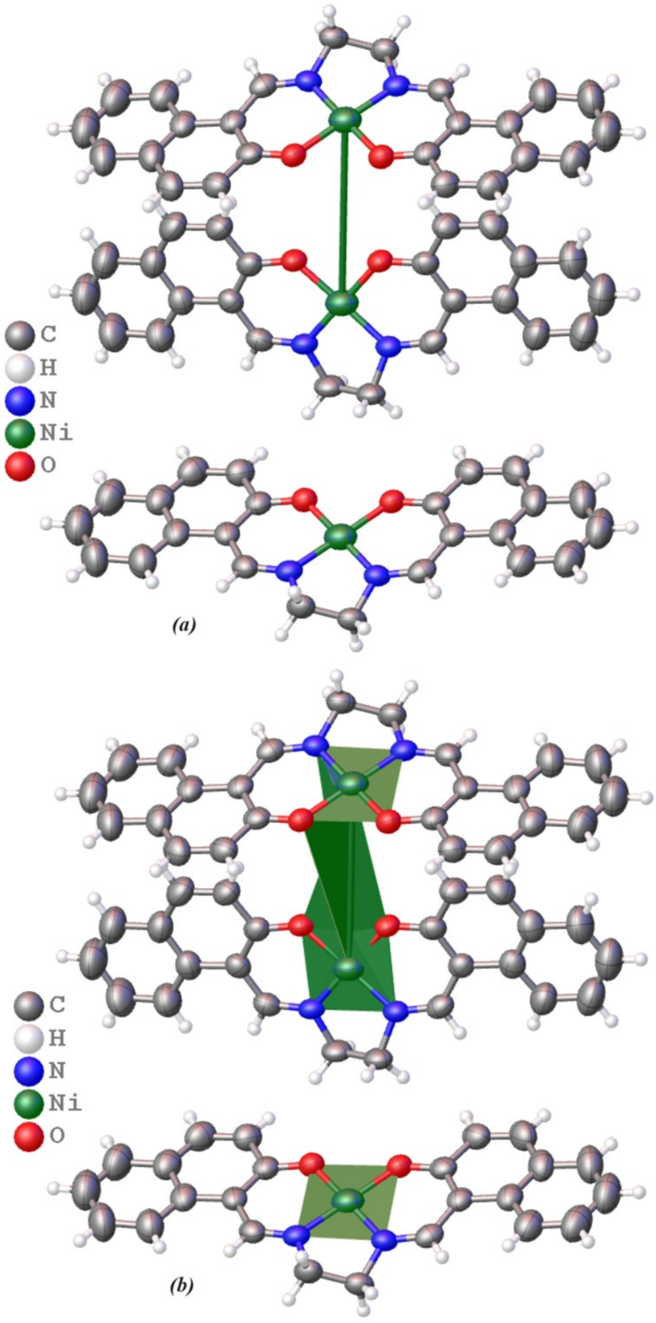

Figure S28. (a) Molecular structure and (b) polyhedron network arrangement for **the** Ni(II) coordination complex $[Ni(L)]_n$(**2**).

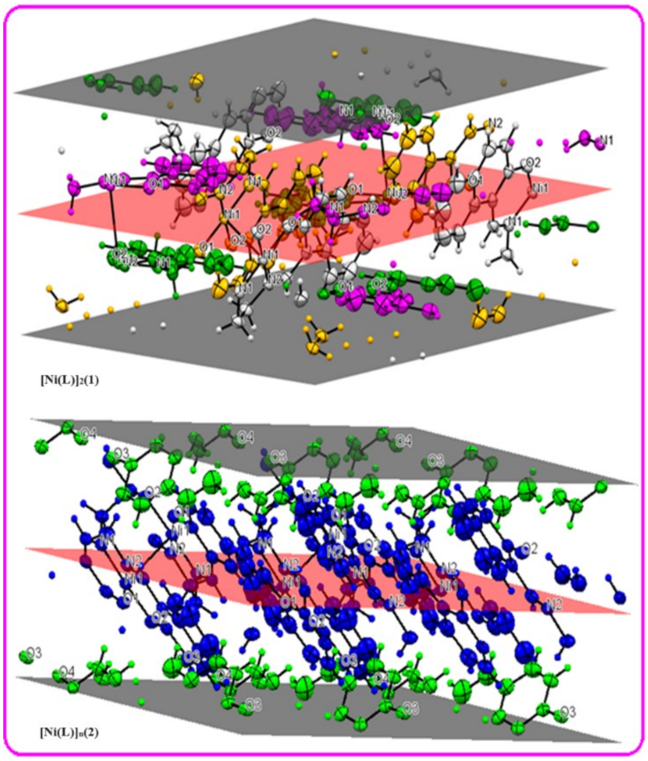

Figure S29. Showing slice view with relative area (0.043) in plane (011) whose the molecules centroid **fitted** for **the** Ni(II) coordination complexes [Ni(L)]$_2$(**1**) and [Ni(L)]$_n$(**2**).

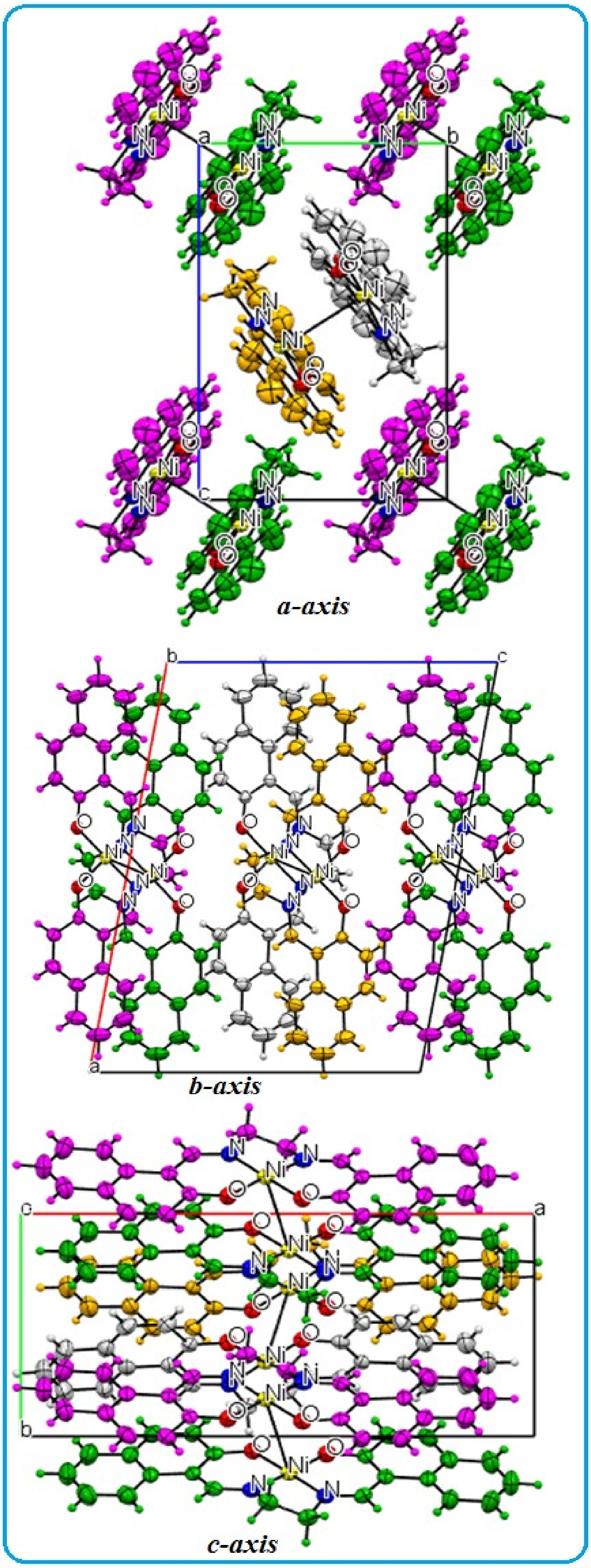

Figure S30. Packing view of **the** Ni(II) coordination complex [Ni(L)]$_2$(**1**) (along the *a*-*c*-axis).

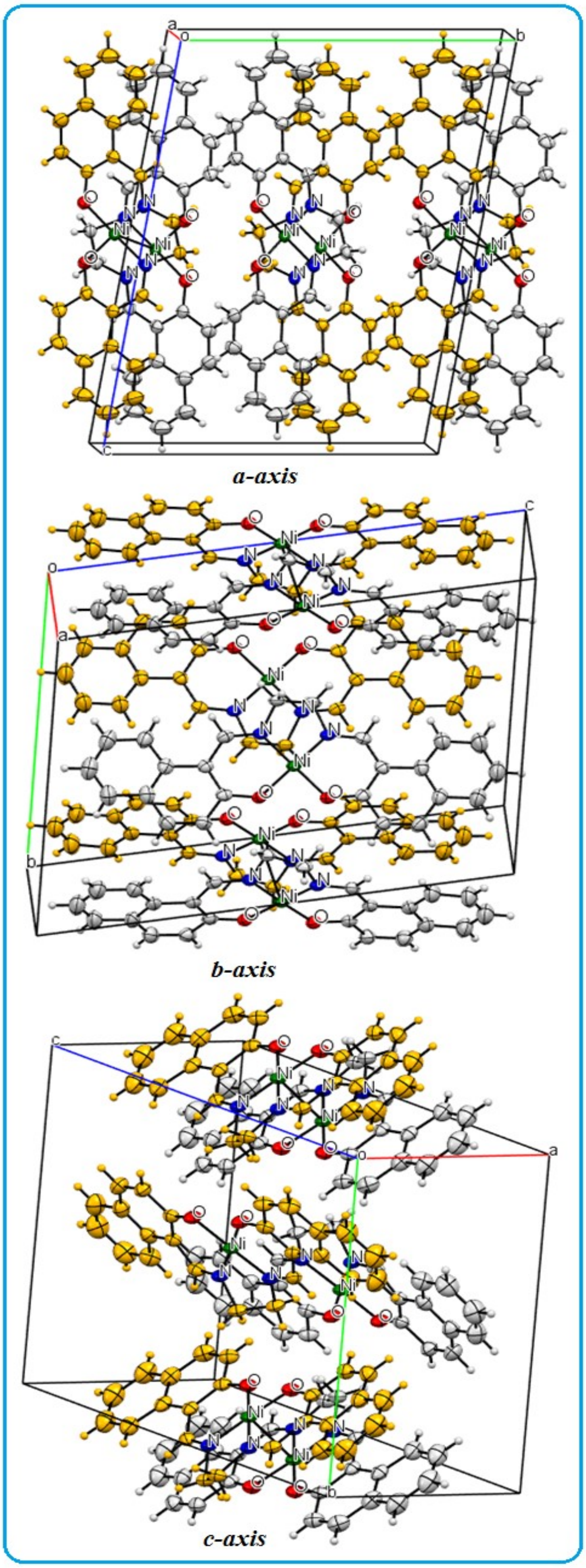

Figure S31. Packing view of **the** Ni(II) coordination complex $[Ni(L)]_n$(**2**) (along the *a*-*c*-axis).

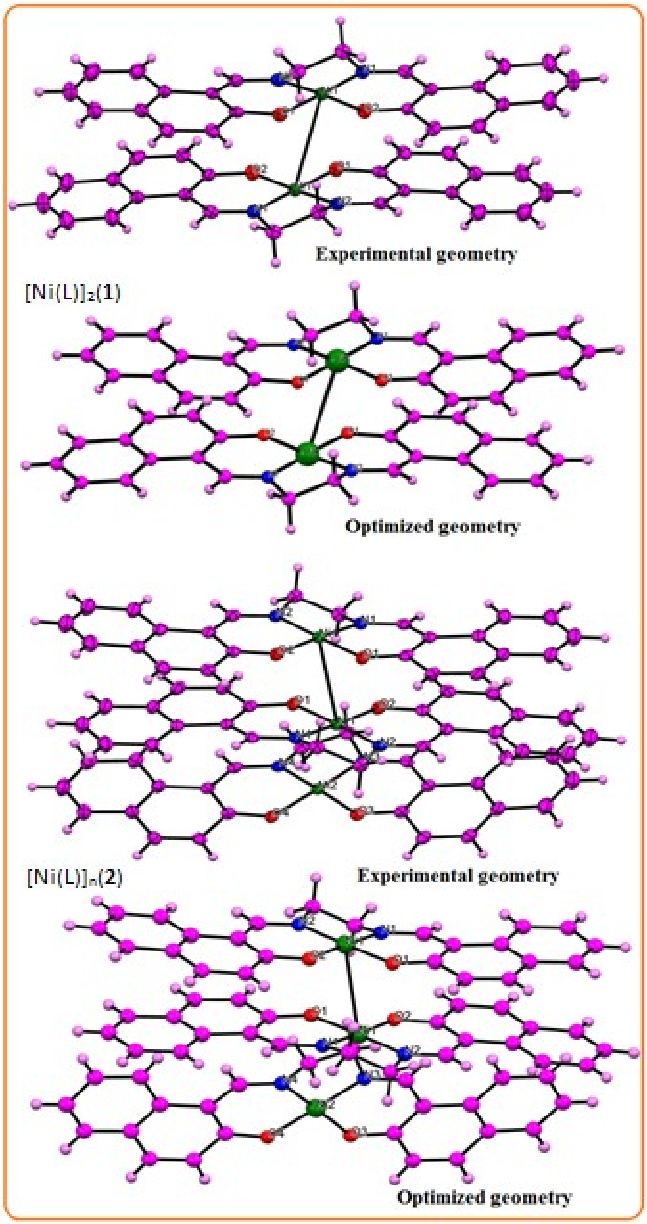

Figure S32. Molecular coordination and optimized geometry of **the** Ni(II) coordination complexes $[Ni(L)]_2$(**1**) and $[Ni(L)]_n$(**2**) determined by using X-ray analysis and DFT method, respectively.

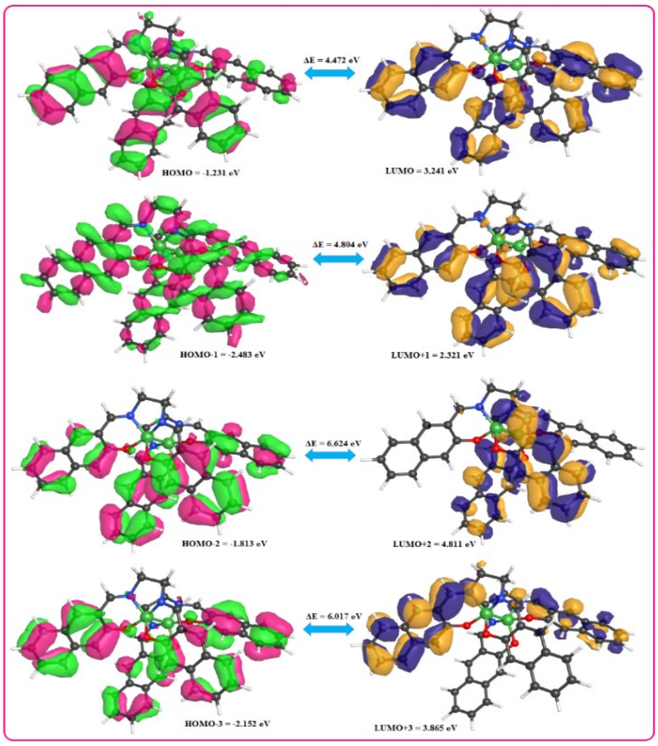

Figure S33. Frontier molecular orbital diagram and energy gap **(ΔE_g) of the** Ni(II) coordination complex $[Ni(L)]_2$(**1**).

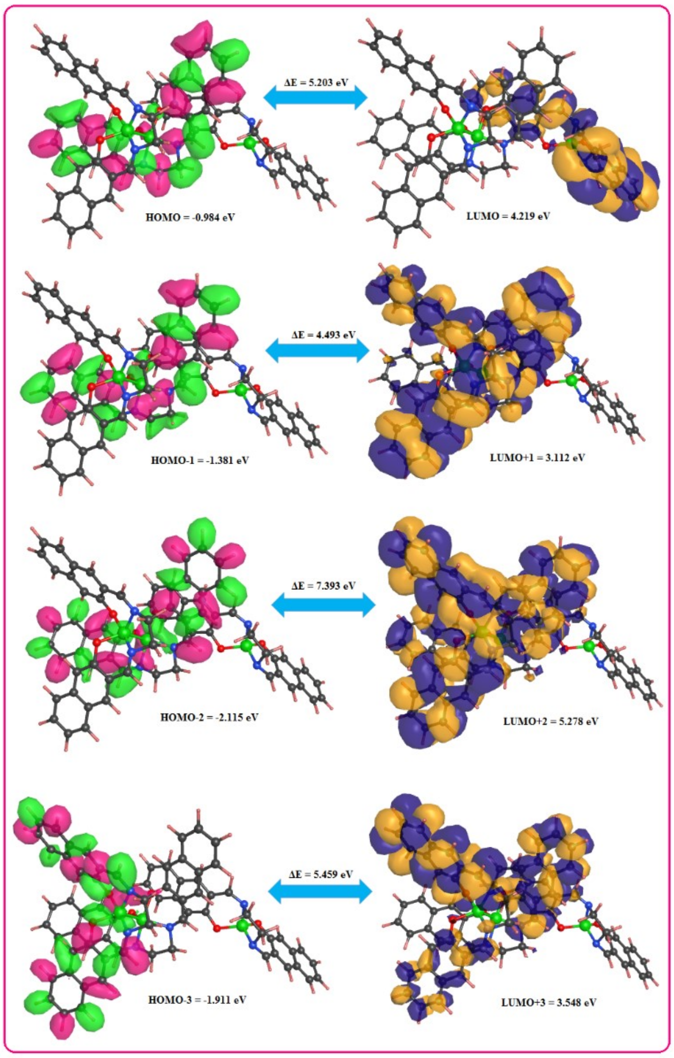

Figure S34. Frontier molecular orbital diagram and energy gap **(ΔE_g) of the** Ni(II) coordination complex $[Ni(L)]_n$(**2**).

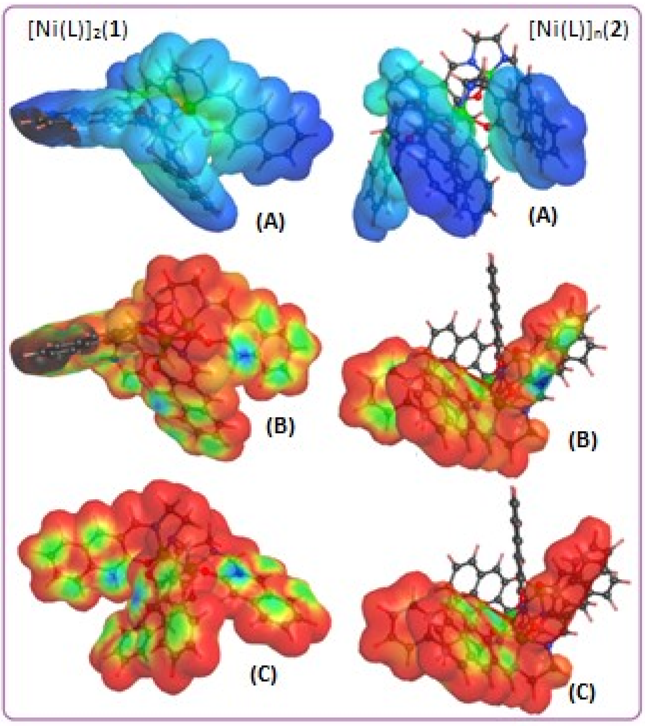

Figure S35. (A) Molecular electrostatic potential (MEPs), (B) Nucleophilic (LUMO) frontier density, and (C) Electrophilic (HOMO) frontier density for the Ni(II) coordination complexes $[Ni(L)]_2$(**1**) and $[Ni(L)]_n$(**2**).

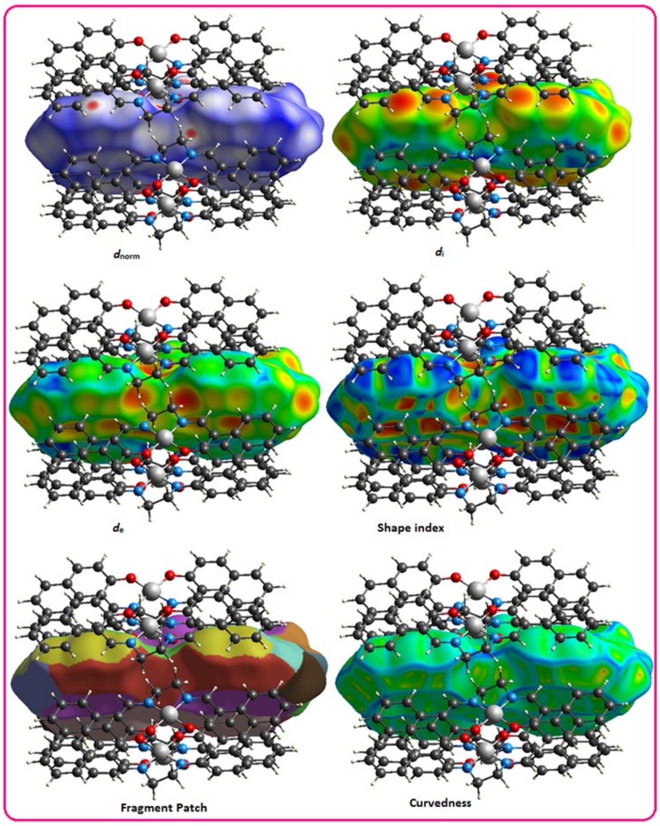

Figure S36. Hirshfeld surfaces mapped with d_{norm}, d_i, d_e, shape index, Fragment patch and curvedness for the Ni(II) coordination complex $[Ni(L)]_n$(**2**) red spots represents the closest contacts and blue colour the most distant contacts for Ni(II) coordination complex $[Ni(L)]_n$(**2**).

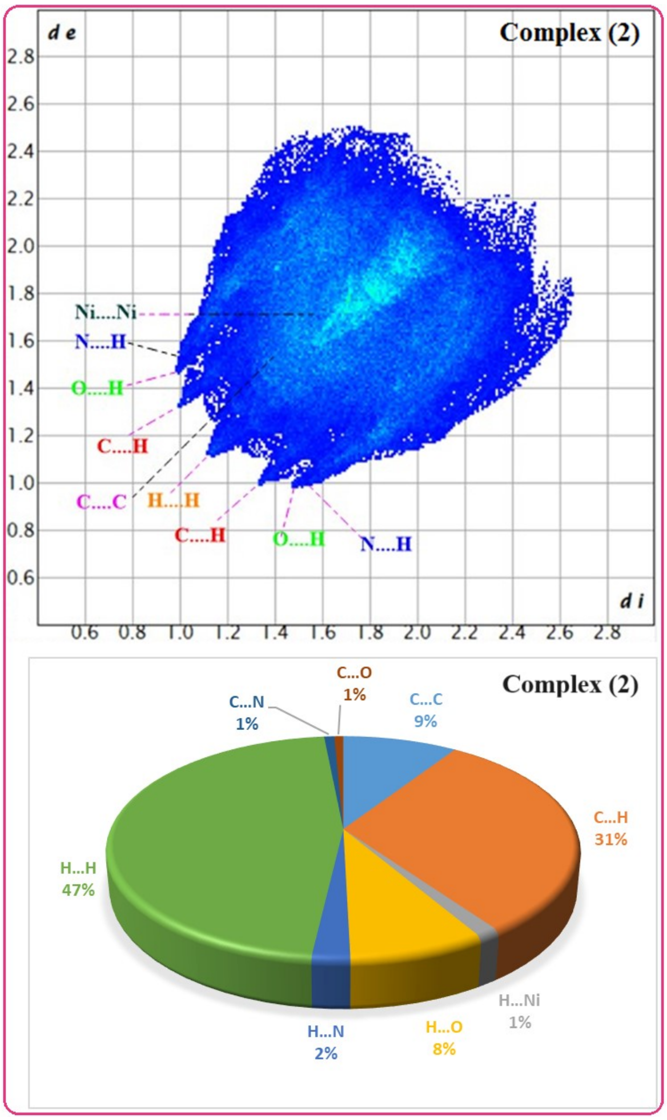

Figure S37. Fingerprint plot for the Ni(II) coordination complex $[Ni(L)]_n$(**2**) showing percentage of contact contributed to the total Hirshfeld surface (HS) area of the molecules and its Pie chart; d_i and d_e are the distances from the surface to the nearest atoms interior and exterior to the surface respectively.

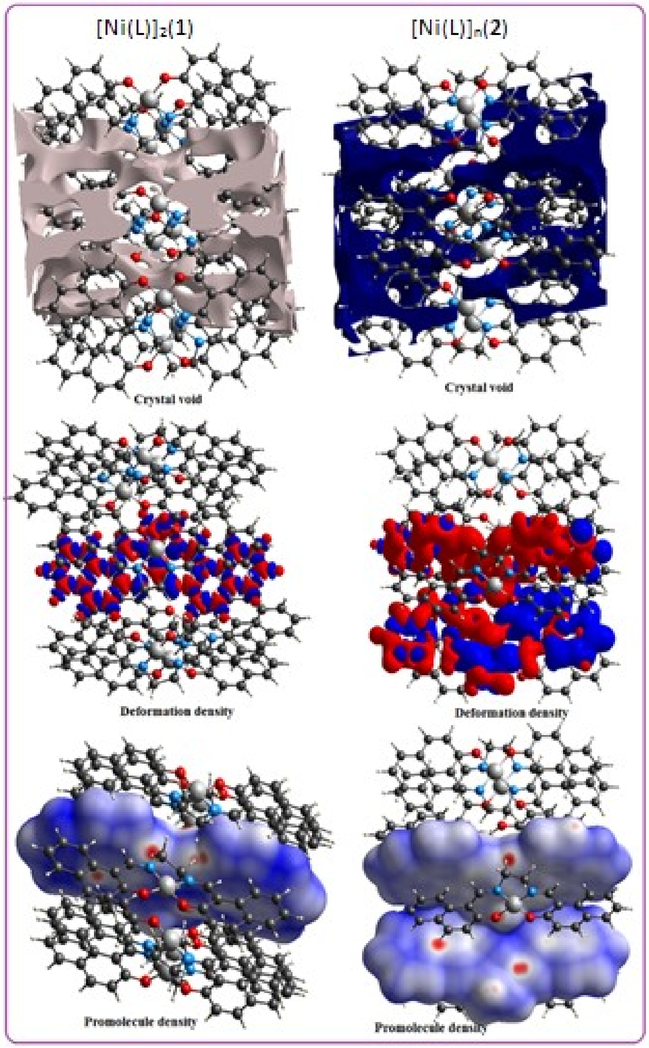

Figure S38. Hirsfeld surface mapped with crystal void, deformation density and promolecule density for **the** Ni(II) coordination complexes $[Ni(L)]_2$(**1**) and $[Ni(L)]_n$(**2**).

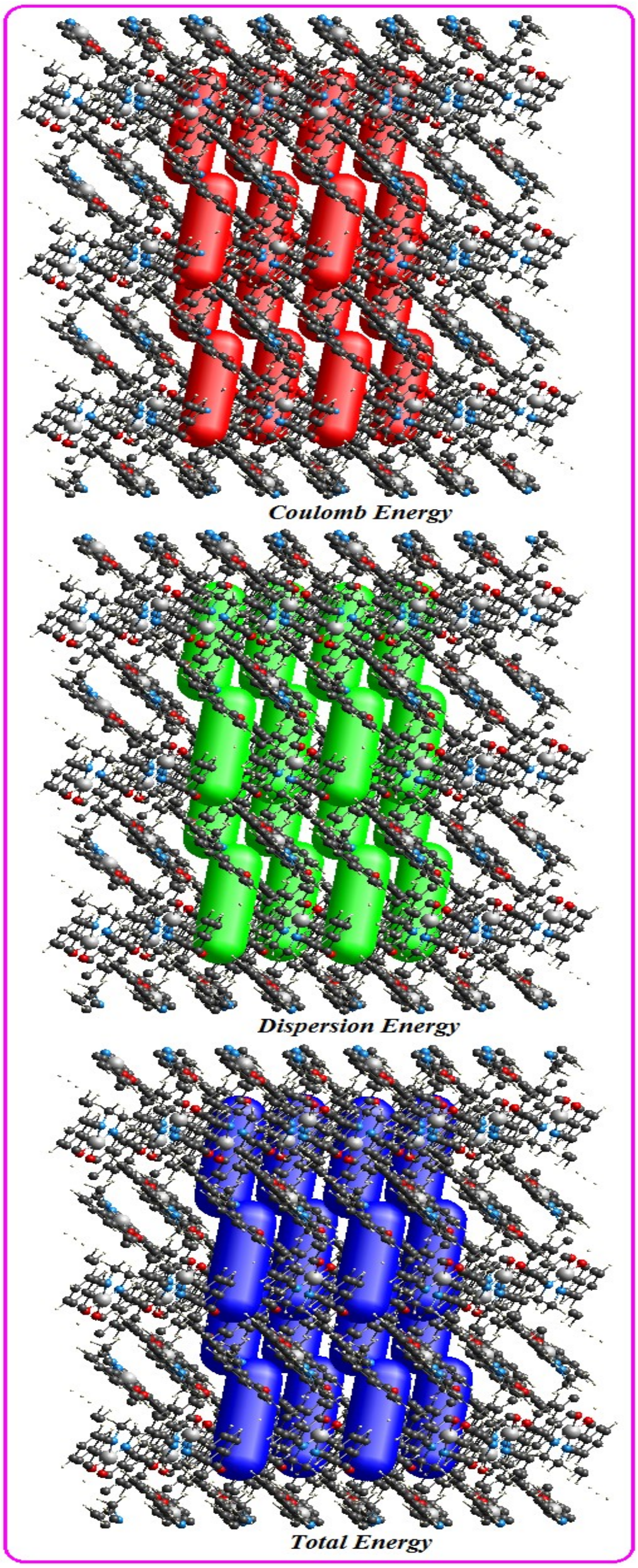

Figure S39. 3D graphical representation of energy framework diagram for **the** Ni(II) coordination complex $[Ni(L)]_n$(**2**). Hydrogen atoms have been omitted for clarity and all diagrams used the same hexagonal scale of 200 for energies.

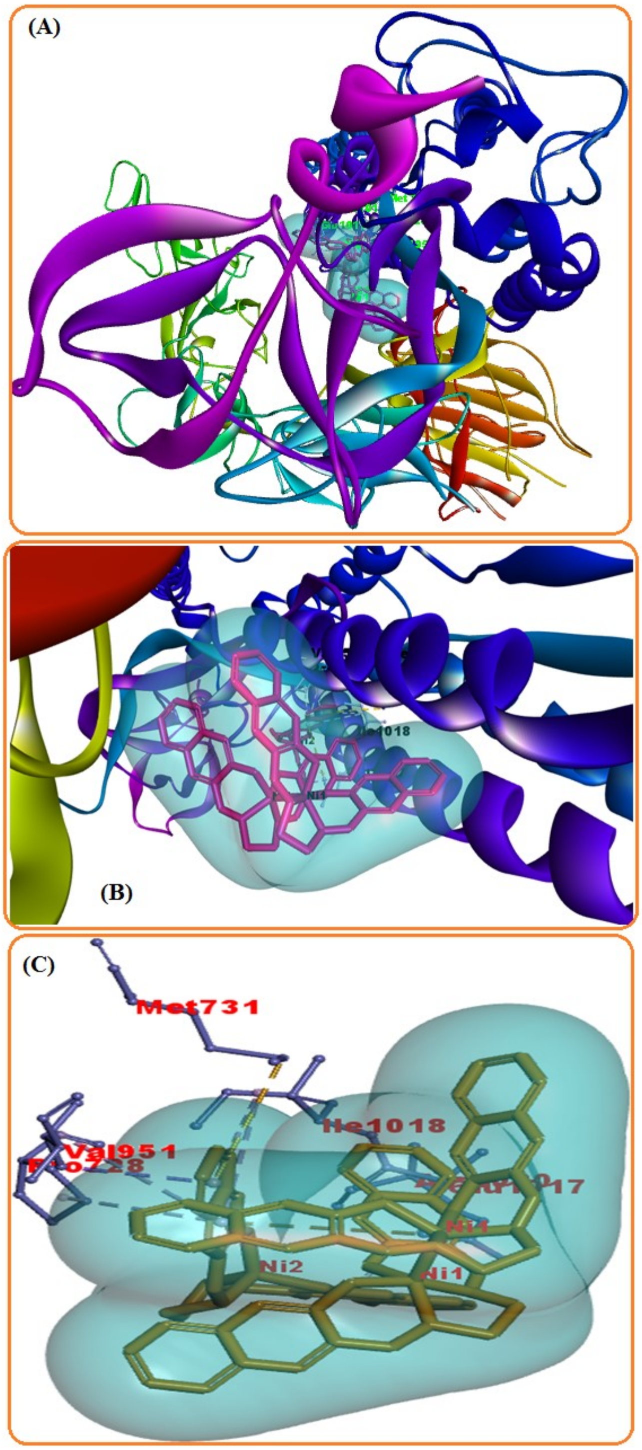

Figure S40. (A) Docked Ni(II) coordination complex $[Ni(L)]_n$(**2**) inside Omicron variant of SARS-CoV-2 (PDB ID: 7WK2); (B) Molecular re-docking of **the** Ni(II) coordination complex $[Ni(L)]_n$(**2**) inside Omicron variant of SARS-CoV-2 focused view for interacting residues and (C) Molecular re-docking of **the** Ni(II) coordination complex $[Ni(L)]_n$(**2**) with metal-ligand interactions inside Omicron variant of SARS-CoV-2 focused view for interacting residues.

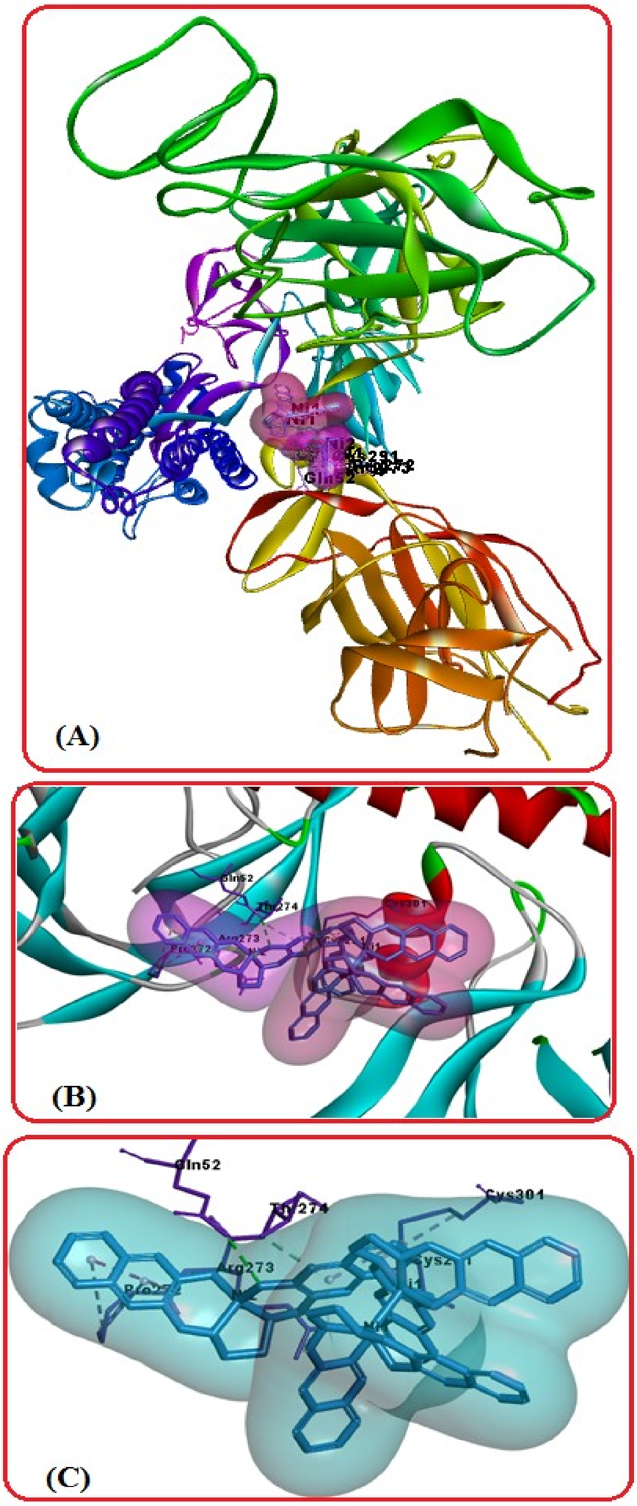

Figure S41. (A) Docked Ni(II) coordination complex $[Ni(L)]_n$(**2**) inside Omicron variant of SARS-CoV-2 (PDB ID: 7WVO); (B) Molecular re-docking of **the** Ni(II) coordination complex $[Ni(L)]_n$(**2**) inside Omicron variant of SARS-CoV-2 focused view for interacting residues; and **(C)** Molecular re-docking of **the** Ni(II) coordination complex $[Ni(L)]_n$(**2**) with metal-ligand interactions inside Omicron variant of SARS-CoV-2 focused view for interacting residues.

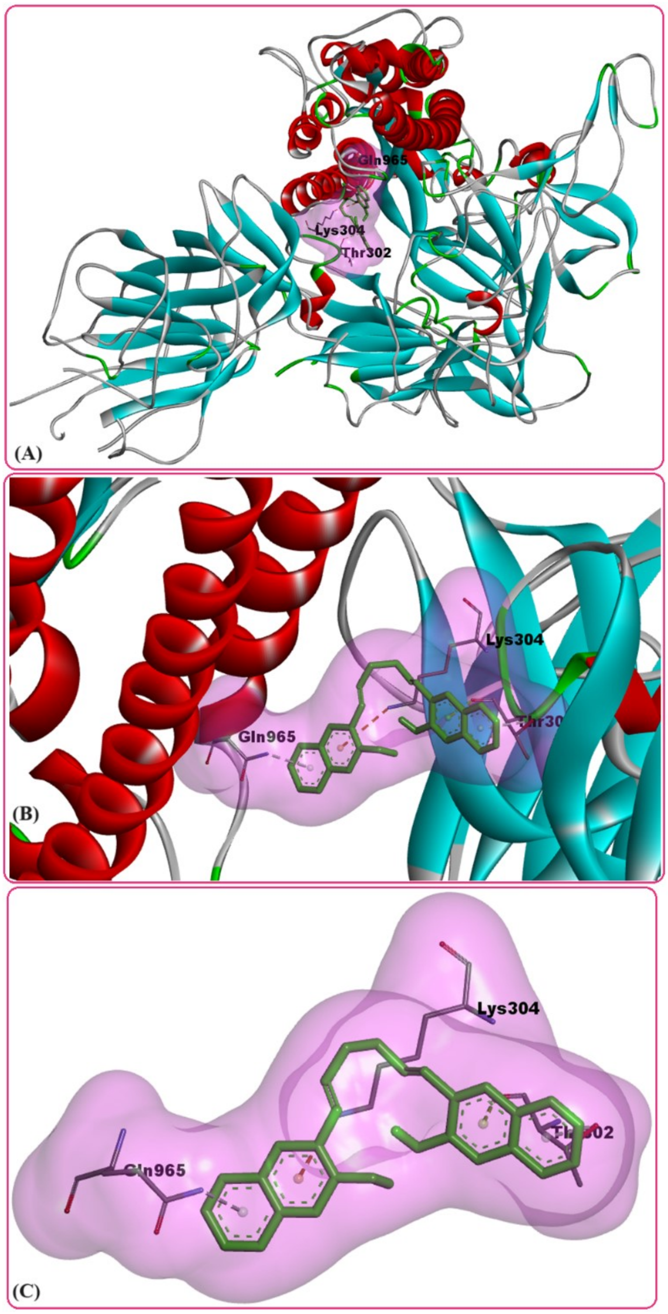

Figure S42. (A) Docked Schiff base ligand (H_2L) inside Omicron variant of SARS-CoV-2 (PDB ID: 7WK2); (B) Molecular re-docking of Schiff base ligand (H_2L) inside Omicron variant of SARS-CoV-2 focused view for interacting residues and (C) Molecular re-docking of Schiff base ligand (H_2L) with ligand interactions inside Omicron variant of SARS-CoV-2 focused view for interacting residues.

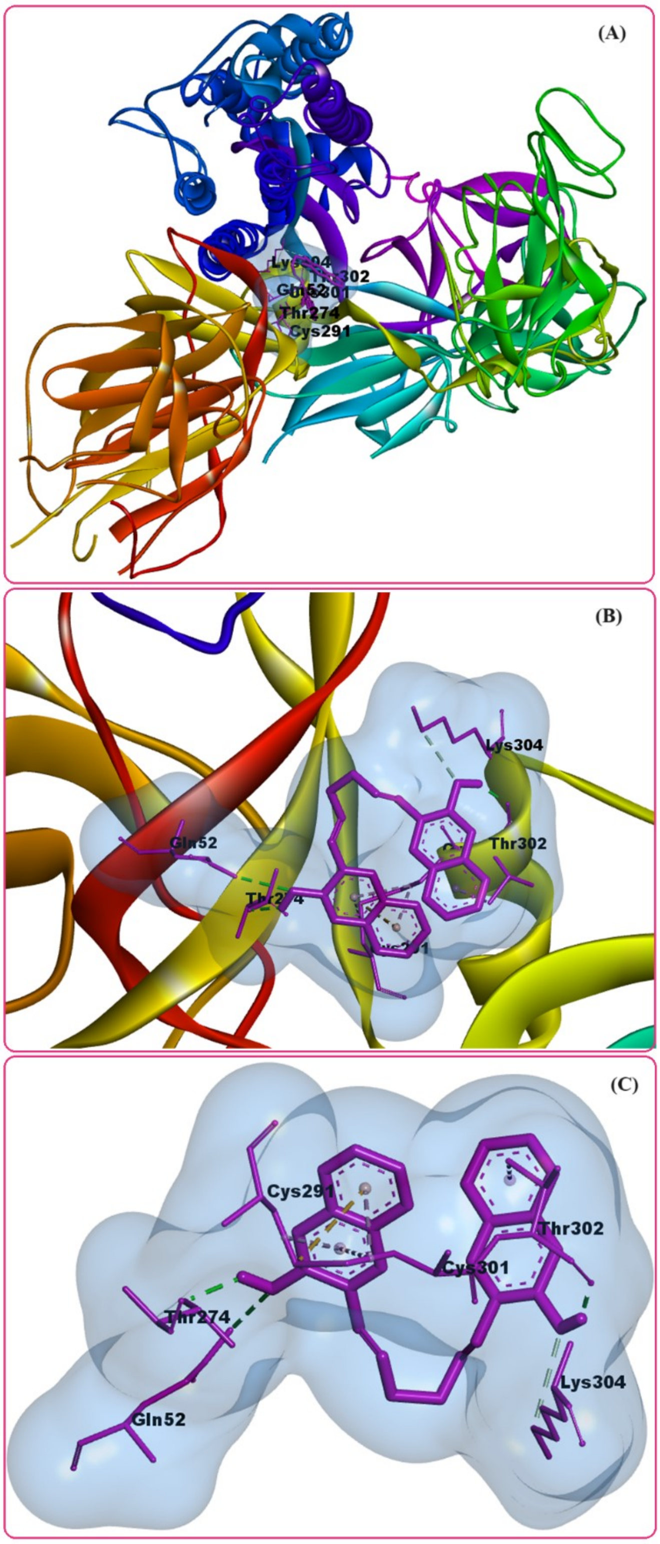

Figure S43. (A) Docked Schiff base ligand (H_2L) inside Omicron variant of SARS-CoV-2 (PDB ID: 7WVO); (B) Molecular re-docking of Schiff base ligand (H_2L) inside Omicron variant of SARS-CoV-2 focused view for interacting residues and (C) Molecular re-docking of Schiff base ligand (H_2L) with ligand interactions inside Omicron variant of SARS-CoV-2 focused view for interacting residues.

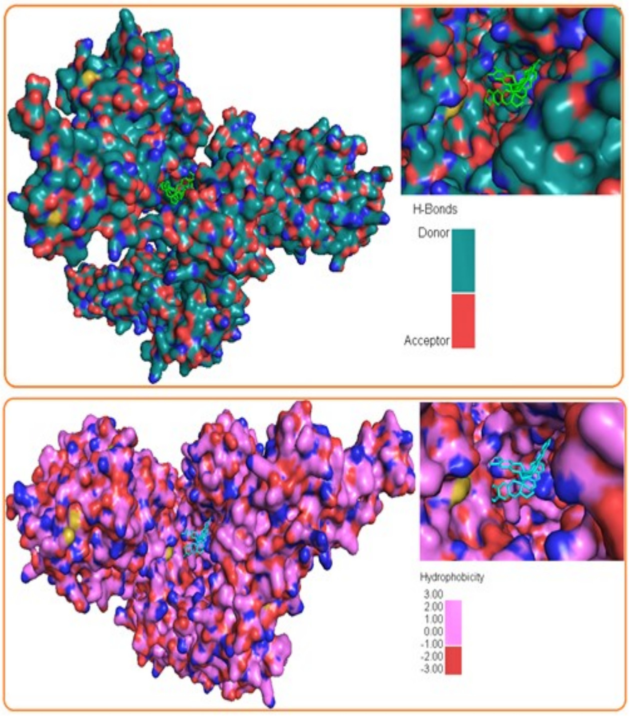

Figure S44. Electrostatic surface representation with H-bonds and Hydrophobicity of docked Ni(II) coordination complex $[Ni(L)]_2$(**1**) inside Omicron variant of SARS-CoV-2 (PDB ID: 7WK2). The ligand (complex) was rendered using the stick representation.

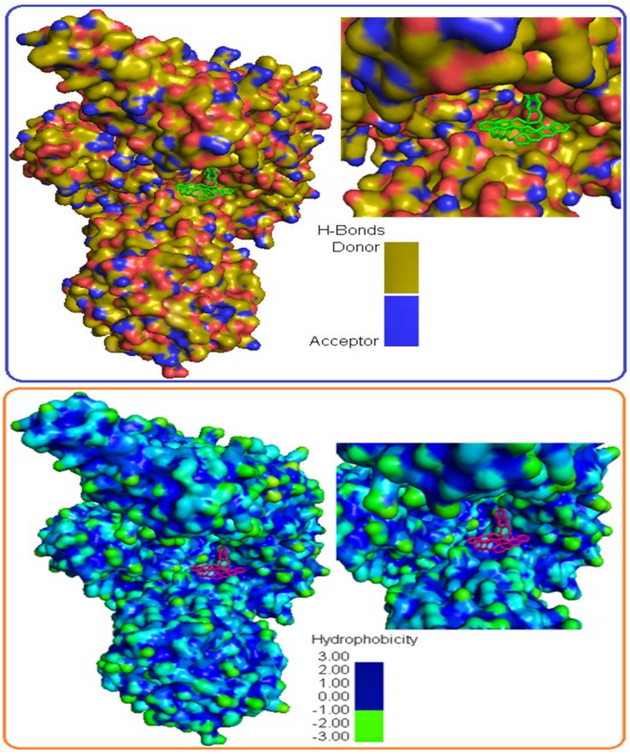

Figure S45. Electrostatic surface representation with H-bonds and Hydrophobicity for docked Ni(II) coordination complex $[Ni(L)]_2$(**1**) inside Omicron variant of SARS-CoV-2 (PDB ID: 7WVO). The ligand (complex) was rendered using the stick representation.

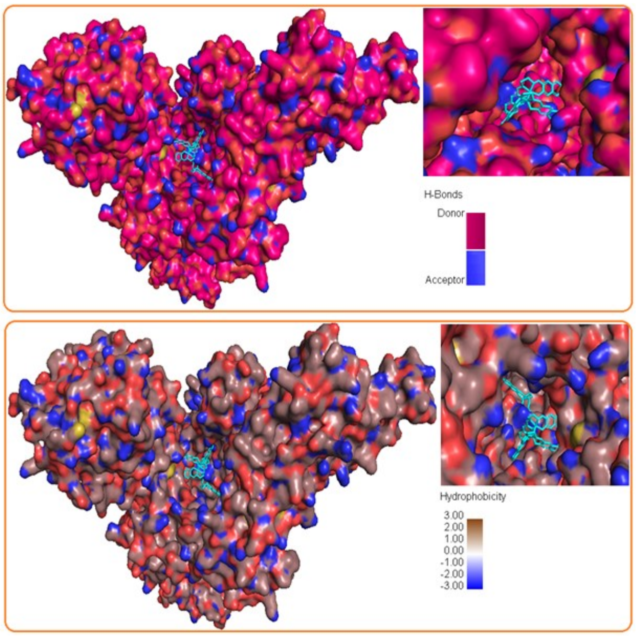

Figure S46. Electrostatic surface representation with H-bonds and Hydrophobicity of docked Ni(II) coordination complex $[Ni(L)]_n$(**2**) inside Omicron variant of SARS-CoV-2 (PDB ID: 7WK2).The ligand (complex) was rendered using the stick representation. Non polar Hydrogen atoms were omitted for clarity.

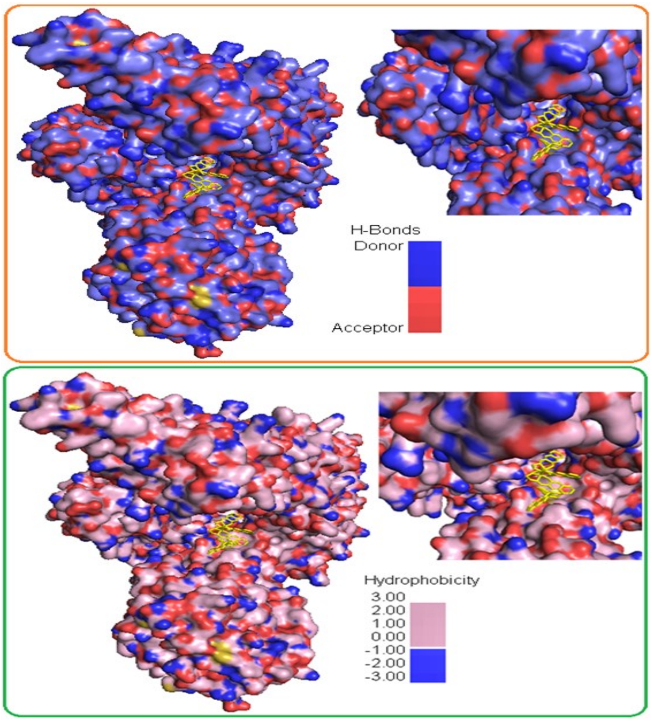

Figure S47. Electrostatic surface representation with H-bonds and Hydrophobicity of docked Ni(II) coordination complex $[Ni(L)]_n$(**2**) inside Omicron variant of SARS-CoV-2 (PDB ID: 7WVO). The ligand (complex) was rendered using the stick representation. Non polar Hydrogen atoms were omitted for clarity.

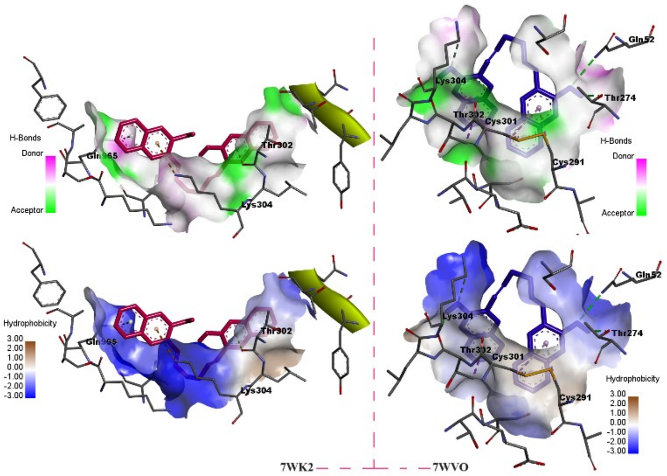

Figure S48. Graphical representation of H-bonds and hydrophobicity of **docked** Schiff base ligand (H_2L) inside Omicron variant of SARS-CoV-2 (PDB ID: 7WK2 and 7WVO).

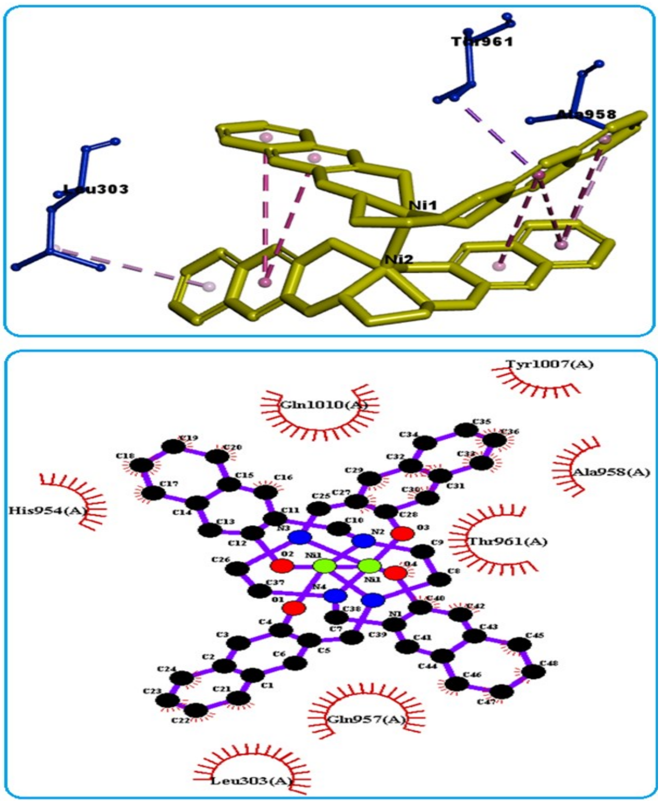

Figure S49. Putative 2D and 3D binding mode, and metal-ligand binding interaction of the Ni(II) coordination complex $[Ni(L)]_2$(**1**) (lime yellow coloured) within active pocket of SARS-CoV-2 Omicron S-open-2 (PDB ID: 7WK2).

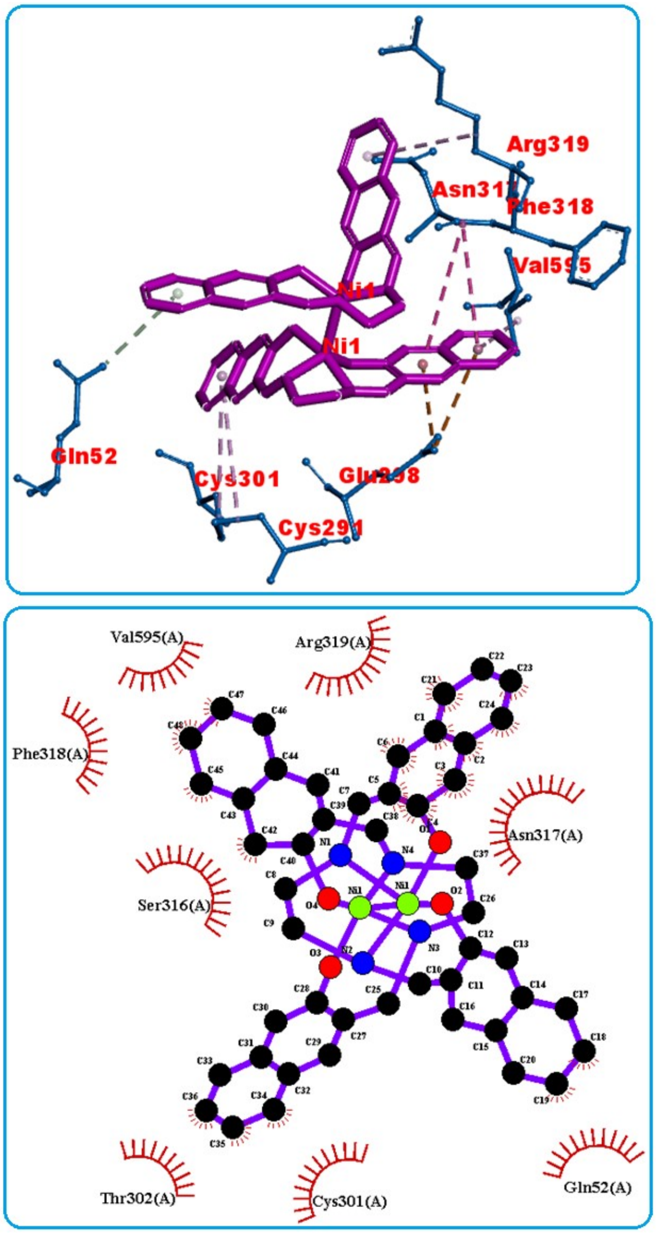

Figure S50. Putative 2D and 3D binding mode, and metal-ligand binding interaction of **the** Ni(II) coordination complex $[Ni(L)]_2$(**1**) (pink coloured) within active pocket of SARS-CoV-2 Omicron S-open-2 (PDB ID: 7WVO).

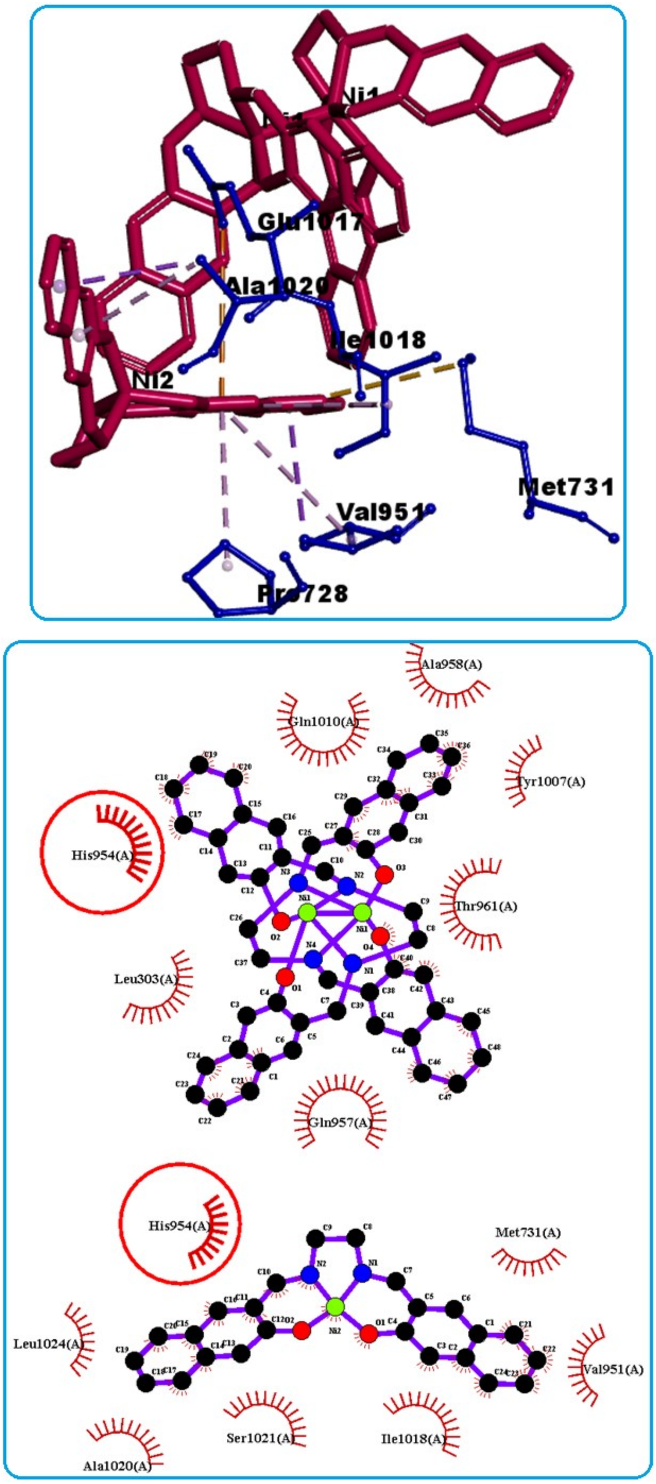

Figure S51. Putative 2D and 3D binding mode, and metal-ligand binding interaction of **the** Ni(II) coordination complex $[Ni(L)]_n$(**2**) (lime yellow coloured) within active pocket of SARS-CoV-2 Omicron S-open-2 (PDB ID: 7WK2).

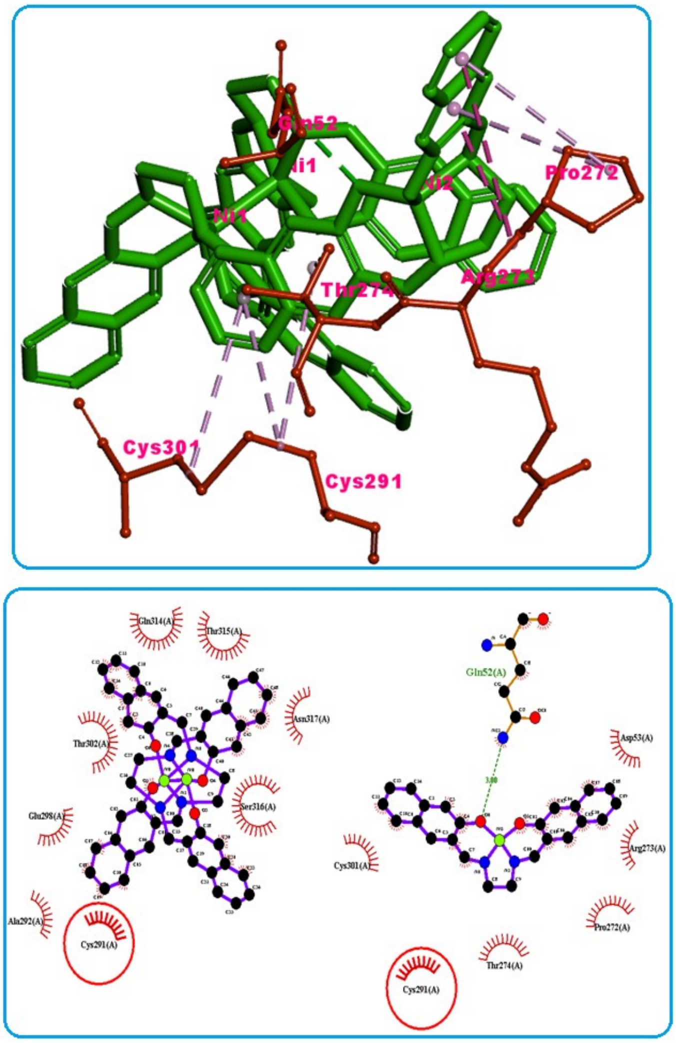

Figure S52. Putative 2D and 3D binding mode, and metal-ligand binding interaction of **the** Ni(II) coordination complex $[Ni(L)]_n$(**2**) (green coloured) within active pocket of SARS-CoV-2 Omicron S-open-2 (PDB ID: 7WVO).

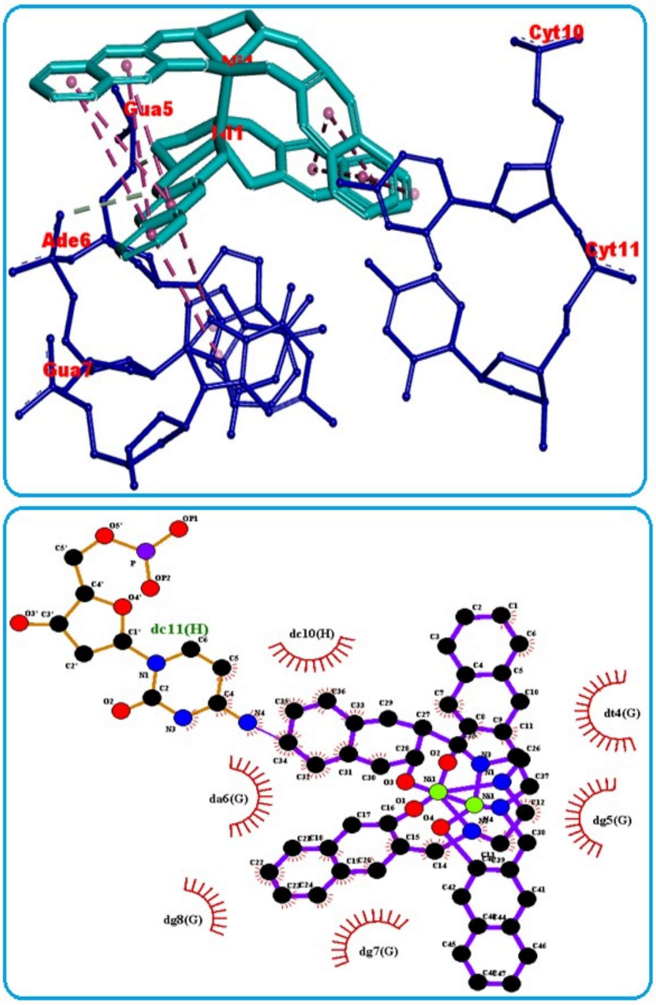

Figure S53. Putative 2D and 3D binding mode, and metal-ligand binding interaction of **the** Ni(II) coordination complex $[Ni(L)]_2$(**1**) (cyan coloured) within active pocket of OSPHR2 in complex with DNA binding protein (PDB ID: 7D3T).

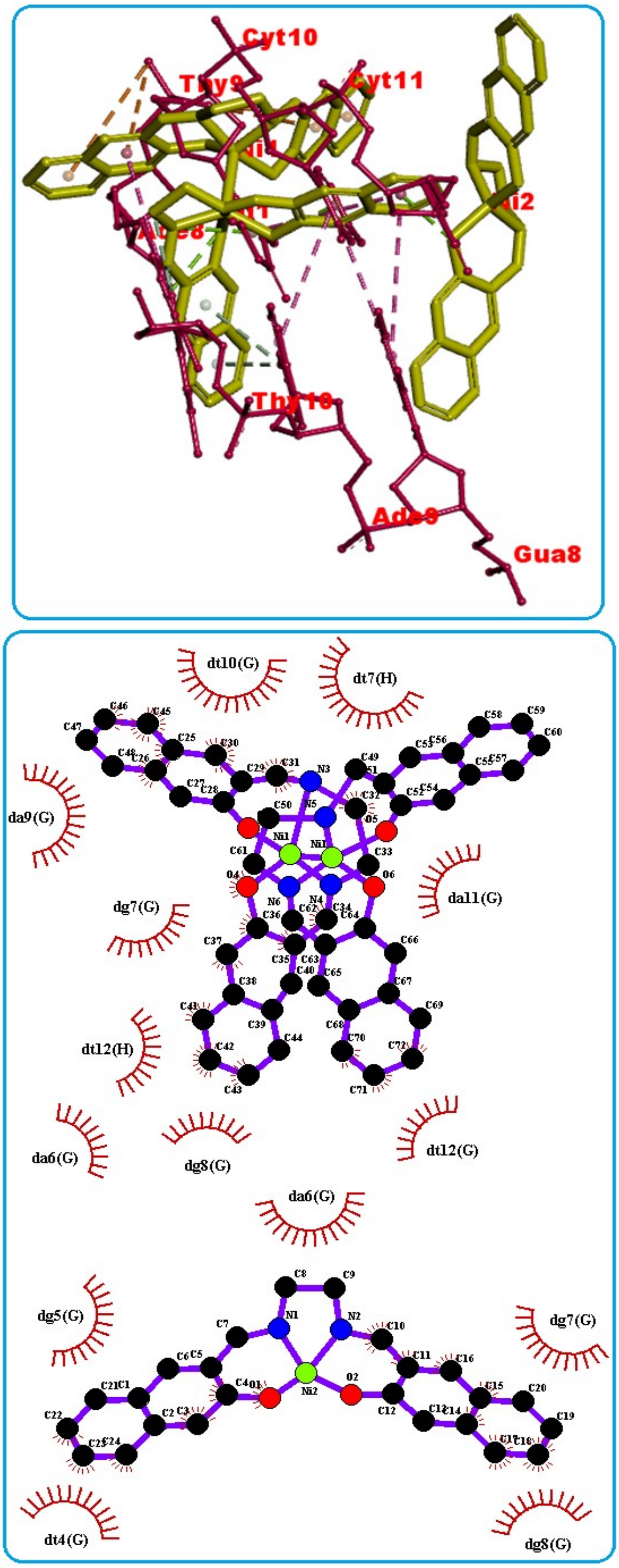

Figure S54. Putative 2D and 3D binding mode, and metal ligand binding interaction of **the** Ni(II) coordination complex $[Ni(L)]_n$(**2**) (lime coloured) within active pocket of OSPHR2 in complex with DNA binding protein (PDB ID: 7D3T).

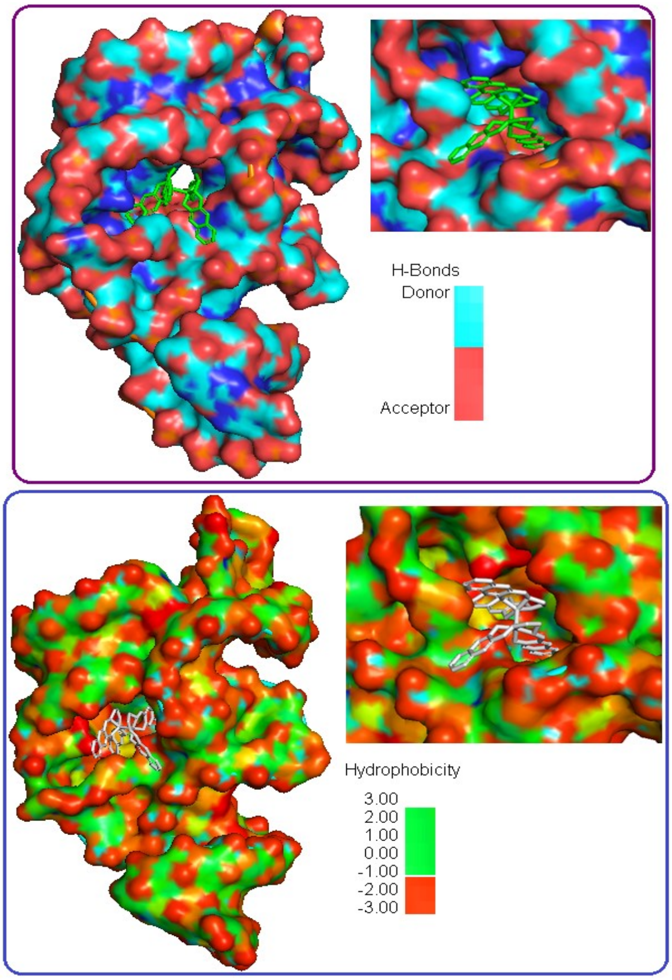

Figure S55. Surface representation with H-bond and hydrophobicity of **the** Ni(II) coordination complex $[Ni(L)]_2$(**1**) (yellow coloured) within active pocket of E. Coli thiM riboswitch in complex with RNA (PDB ID: 7TDC).

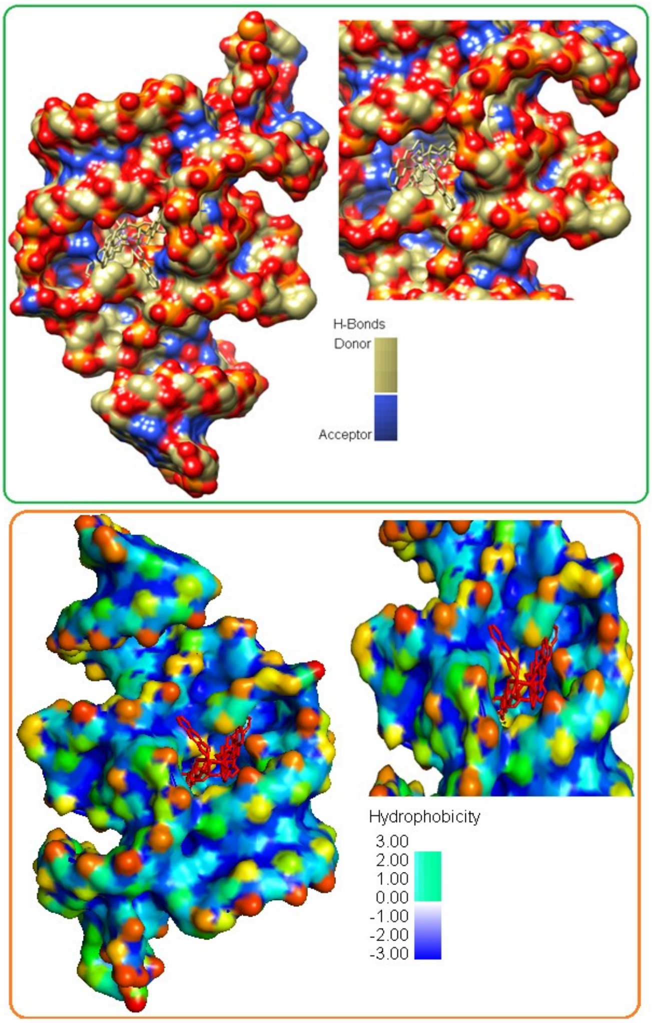

Figure S56. Surface representation with H-bond and hydrophobicity of **the** Ni(II) coordination complex $[Ni(L)]_n$(**2**) (yellow coloured) within active pocket of E. Coli thiM riboswitch in complex with RNA (PDB ID: 7TDC).

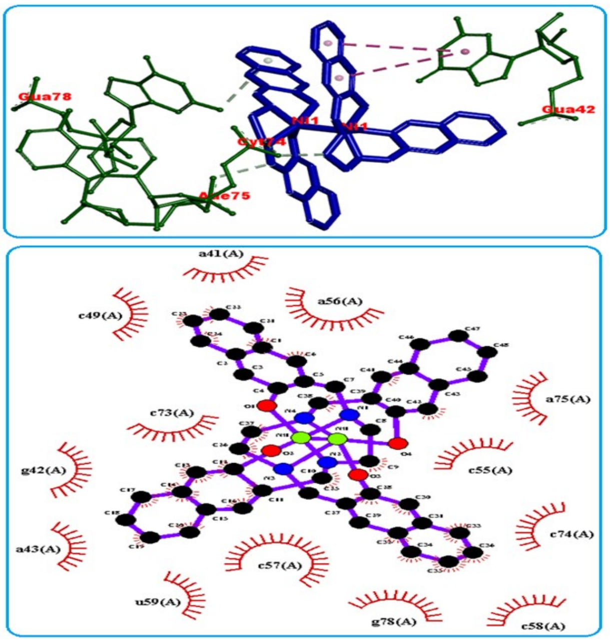

Figure S57. Putative 2D and 3D binding mode, and metal-ligand binding interaction of **the** Ni(II) coordination complex $[Ni(L)]_2$(**1**) (blue coloured) within active pocket of E. Coli thiM riboswitch in complex with RNA (PDB ID: 7TDC).

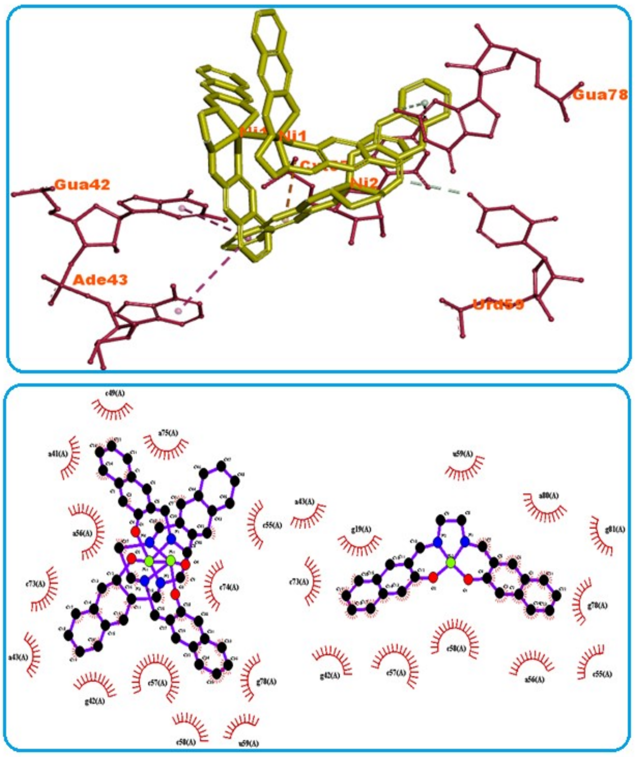

Figure S58. Putative 2D and 3D binding mode, and metal-ligand binding interaction of **the** Ni(II) coordination complex $[Ni(L)]_n$(**2**) (yellow coloured) within active pocket of E. Coli thiM riboswitch in complex with RNA (PDB ID: 7TDC).

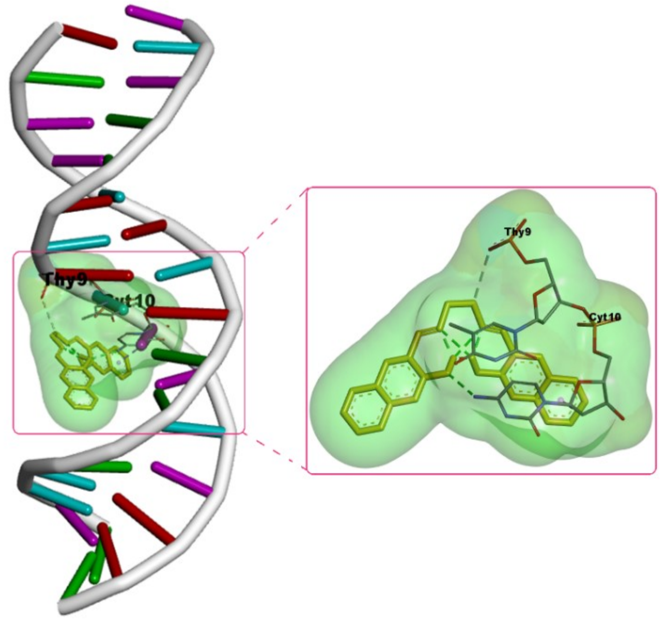

Figure S59. Molecular docking and binding interactions of Schiff base ligand (H_2L) within active pocket of OSPHR2 in complex with DNA binding protein (PDB ID: 7D3T).

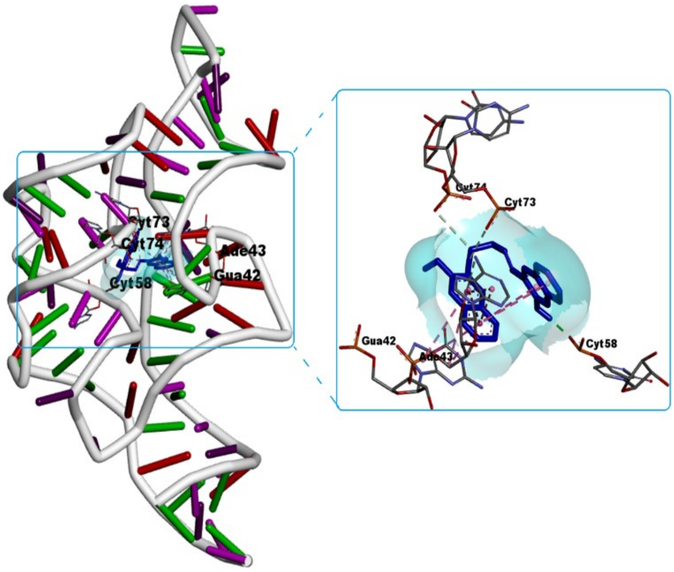

Figure S60. Molecular docking and binding interactions of Schiff base ligand (H_2L) within active pocket of E. Coli thiM riboswitch in complex with RNA (PDB ID: 7TDC).

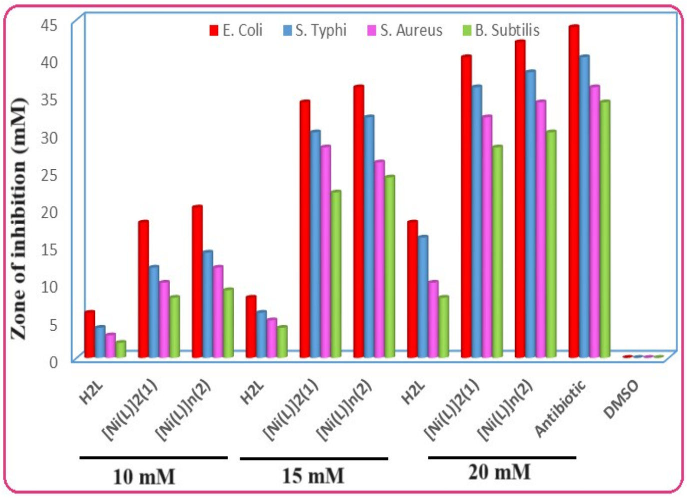

Figure S61. Graphical representation of antibacterial screening activity of the Schiff base ligand (H_2L) and the dimer Ni(II) complexes $[Ni(L)]_2$(**1**) and $[Ni(L)]_n$(**2**) against G(-) and G(+) baterial strains of microorganisms at different concentrations (10-20 mM) .

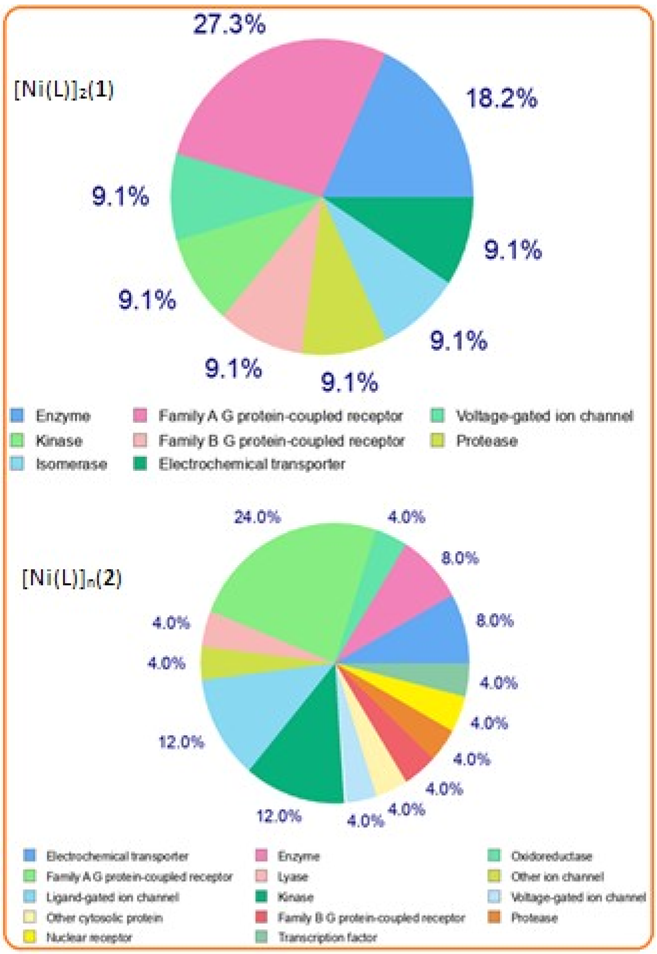

Figure S62. Pie chart representation for **the** Ni(II) coordination complexes $[Ni(L)]_2$(**1**) and $[Ni(L)]_n$(**2**) with Swiss-target predictions.

Table S1. Electrochemical cyclic voltammetry data for **the** Ni(II) coordination complexes $[Ni(L)]_2$(**1**) and $[Ni(L)]_n$(**2**) in DMSO solution containing 1M-TBAP as supporting electrolytes at different scan rates.

Scan rate (m V/s)	E_{pc} (mV)	I_{pc} (μA)	E_{pa} (mV)	I_{pa} (μA)	ΔE_p (mV)	E'_0 (mV)	I_{pa}/I_p (μA)
(**1**)							
10	-0.030	-2.772	0.072	3.550	0.102	0.021	-0.280
20	-0.094	-3.695	0.119	2.934	0.213	0.012	-0.794
50	-0.111	7.546	-0.192	2.626	-0.081	-0.151	0.347
(**2**)							
10	-0.128	-3.775	-0.012	2.421	0.116	-0.071	-0.641
20	-0.123	-4.218	-0.136	2.231	-0.013	-0.130	-0.528
50	-0.171	7.560	-0.141	2.213	0.030	-0.156	0.292
100	-0.213	-2.131	-0.153	-8.605	-0.060	-0.183	4.038

$\Delta E_p = E_{pa} - E_{pc}$; $E'_0(mV) = (E_{pa} + E_{pc})/2$

Table S2. Hydrogen bond parameters found in **the** Ni(II) coordination complexes $[Ni(L)]_2$(**1**) and $[Ni(L)]_n$(**2**).

D-H···A	**D-H (Å)**	**H···A (Å)**	**D···A (Å)**	**<D-H-A (°)**	**Symmetry**
		Complex $[Ni(L)]_2$(**1**)			
C13-H13A···O2	1.080	2.394	3.313	142.07	x,-y+1/2+1,+z+1/2
C12-H12B···O2	1.080	2.708	3.419	123.03	-x+1,-y+1,-z+1
C12-H12B···O1	1.080	2.439	3.242	130.14	-x+1,-y+1,-z+1
C13-H13B···N2	1.080	2.579	3.634	165.04	-x+1,-y+2,-z+1
		Complex $[Ni(L)]_n$(**2**)			
C34-H34B···O2	1.080	2.360	3.285	142.77	x, y, z
C12-H12A···N1	1.080	2.482	3.543	167.34	-x+2,-y,-z+1
C12-H12B···O3	1.080	2.419	3.342	142.62	x,+y-1,+z
C13-H13A···O1	1.080	2.544	3.276	124.30	-x+1,-y,-z+1
C13-H13A···O2	1.080	2.615	3.311	121.53	-x+1,-y,-z+1
C34-H34A···N4	1.080	2.673	3.714	161.58	-x+1,-y+1,-z+1
C35-H35A···O4	1.080	2.354	3.202	134.27	-x+2,-y+1,-z+1
C35-H35A···O3	1.080	2.792	3.511	123.89	-x+2,-y+1,-z+1
C45-H45···O2	1.080	2.858	3.759	140.98	-x+2,-y+1,-z+1

Table S3. Energy framework CE-B3LYP estimates of energy components and total energies (kJ/mol) for the closest intermolecular interactions in the Ni(II) complexes $[Ni(L)]_2$(**1**) and $[Ni(L)]_n$(**2**).

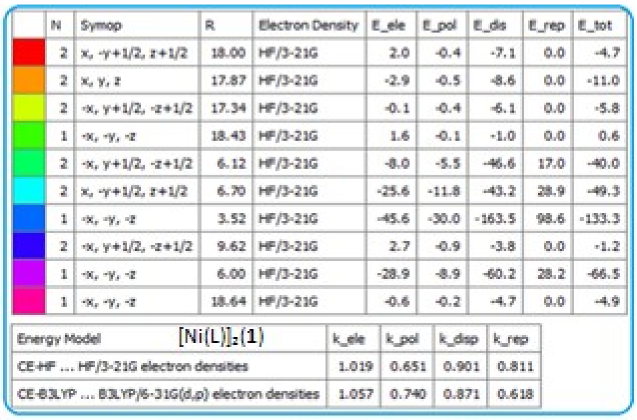

	N	Symop	R	Electron Density	E_ele	E_pol	E_dis	E_rep	E_tot
🟥	2	x, -y+1/2, z+1/2	18.00	HF/3-21G	2.0	-0.4	-7.1	0.0	-4.7
🟧	2	x, y, z	17.87	HF/3-21G	-2.9	-0.5	-8.6	0.0	-11.0
🟨	2	-x, y+1/2, -z+1/2	17.34	HF/3-21G	-0.1	-0.4	-6.1	0.0	-5.8
🟩	1	-x, -y, -z	18.43	HF/3-21G	1.6	-0.1	-1.0	0.0	0.6
🟩	2	-x, y+1/2, -z+1/2	6.12	HF/3-21G	-8.0	-5.5	-46.6	17.0	-40.0
🟦	2	x, -y+1/2, z+1/2	6.70	HF/3-21G	-25.6	-11.8	-43.2	28.9	-49.3
🟦	1	-x, -y, -z	3.52	HF/3-21G	-45.6	-30.0	-163.5	98.6	-133.3
🟦	2	-x, y+1/2, -z+1/2	9.62	HF/3-21G	2.7	-0.9	-3.8	0.0	-1.2
🟪	1	-x, -y, -z	6.00	HF/3-21G	-28.9	-8.9	-60.2	28.2	-66.5
🟪	1	-x, -y, -z	18.64	HF/3-21G	-0.6	-0.2	-4.7	0.0	-4.9

Energy Model $[Ni(L)]_2$(**1**)	k_ele	k_pol	k_disp	k_rep
CE-HF … HF/3-21G electron densities	1.019	0.651	0.901	0.811
CE-B3LYP … B3LYP/6-31G(d,p) electron densities	1.057	0.740	0.871	0.618

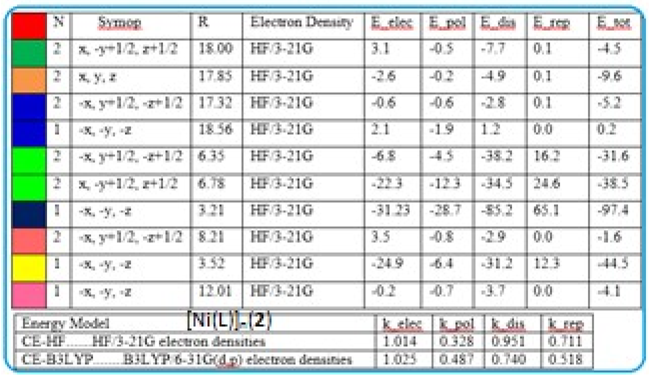

🟥	N	Symop	R	Electron Density	E_elec	E_pol	E_dis	E_rep	E_tot
🟩	2	x, -y+1/2, z+1/2	18.00	HF/3-21G	3.1	-0.5	-7.7	0.1	-4.5
🟧	2	x, y, z	17.85	HF/3-21G	-2.6	-0.2	-4.9	0.1	-9.6
🟦	2	-x, y+1/2, -z+1/2	17.32	HF/3-21G	-0.6	-0.6	-2.8	0.1	-5.2
🟦	1	-x, -y, -z	18.56	HF/3-21G	2.1	-1.9	1.2	0.0	0.2
🟩	2	-x, y+1/2, -z+1/2	6.35	HF/3-21G	-6.8	-4.5	-38.2	16.2	-31.6
🟩	2	x, -y+1/2, z+1/2	6.78	HF/3-21G	-22.3	-12.3	-34.5	24.6	-38.5
🟦	1	-x, -y, -z	3.21	HF/3-21G	-31.23	-28.7	-85.2	65.1	-97.4
🟥	2	-x, y+1/2, -z+1/2	8.21	HF/3-21G	3.5	-0.8	-2.9	0.0	-1.6
🟨	1	-x, -y, -z	3.52	HF/3-21G	-24.9	-6.4	-31.2	12.3	-44.5
🟪	1	-x, -y, -z	12.01	HF/3-21G	-0.2	-0.7	-3.7	0.0	-4.1

Energy Model $[Ni(L)]_n$(**2**)	k_elec	k_pol	k_dis	k_rep
CE-HF……HF/3-21G electron densities	1.014	0.328	0.951	0.711
CE-B3LYP……B3LYP/6-31G(d,p) electron densities	1.025	0.487	0.740	0.518

Table S4. Established structure activity relationship (SAR) between the experimental geometries of the Ni**(II)** dimer complexes $[Ni(L)]_2$(**1**) and $[Ni(L)]_n$(**2**) determined by the single crystal X-ray diffraction technique and the theoretical geometries observed upon interactions against SARS-CoV-2 Omicron variants (PDB ID: 7WK2 and 7WVO).

Complexes	Experimental bond lengths (Å)		Docked complexes inside SARS-CoV-2 Omicron variant with bond lengths (Å)			
			PDB ID: 7WK2		PDB ID: 7WVO	
$[Ni(L)]_2$(**1**)	Ni(1)-O(1)	1.861(2)	Ni(1)-O(1)	1.832(1)	Ni(1)-O(1)	1.866(11)
	Ni(1)-O(2)	1.860(2)	Ni(1)-O(2)	1.854(3)	Ni(1)-O(2)	1.861(4)
	Ni(1)-N(1)	1.855(3)	Ni(1)-N(1)	1.823(5)	Ni(1)-N(1)	1.842(6)
	Ni(1)-N(2)	1.856(3)	Ni(1)-N(2)	1.833(13)	Ni(1)-N(2)	1.866(4)
$[Ni(L)]_n$(**2**)	Ni(1)-O(1)	1.863(2)	Ni(1)-O(1)	1.855(12)	Ni(1)-O(1)	1.866(1)
	Ni(1)-O(2)	1.922(2)	Ni(1)-O(2)	1.913(6)	Ni(1)-O(2)	1.921(2)
	Ni(1)-N(1)	1.907(3)	Ni(1)-N(1)	1.923(12)	Ni(1)-N(1)	1.908(6)
	Ni(1)-N(2)	1.855(3)	Ni(1)-N(2)	1.846(13)	Ni(1)-N(2)	1.861(4)
	Ni(2)-O(3)	1.807(2)	Ni(2)-O(3)	1.814(11)	Ni(2)-O(3)	1.826(1)
	Ni(1)-O(4)	1.862(2)	Ni(1)-O(4)	1.863(12)	Ni(1)-O(4)	1.854(1)
	Ni(1)-N(3)	1.856(3)	Ni(1)-N(3)	1.861(12)	Ni(1)-N(3)	1.861(2)
	Ni(1)-N(4)	1.803(3)	Ni(1)-N(4)	1.821(1)	Ni(1)-N(4)	1.823(11)

Table S5. Pharmacokinetic properties of the Ni(II) coordination complexes $[Ni(L)]_2$(**1**) and $[Ni(L)]_n$(**2**).

Property	Model Name	Predicted Values for complexes	
		$[Ni(L)]_2$(**1**)	$[Ni(L)]_n$(**2**)
Absorption	Water solubility(log mol/L)	-4.205	-5.571
	$Caco_2$ permeability(log Papp in 10^{-6} cm/s)	0.897	1.227
	Intestinal absorption (human) (%Absorbed)	98.254	90.982
	Skin Permeability(Log Kp)	-2.154	-3.413
	P-glycoprotein Substrate	No	No
	P-glycoprotein I inhibitor	Yes	Yes
	P-glycoprotein II inhibitor	Yes	Yes
Distribution	VDss (human) (log L/kg)	-0.781	-0.811
	Fraction unbound (human) (Fu)	0.407	0.409
	BBB permeability(log BB)	-1.104	-1.109
	CNS permeability(log PS)	-0.788	-0.798
Metabolism	CYP2D6 substrate	No	No
	CYP3A4 substrate	Yes	Yes
	CYP1A2 substrate	Yes	Yes
	CYP2C19 inhibitor	Yes	Yes
	CYP2C9 inhibitor	Yes	Yes
	CYP2D6 inhibitor	No	No
	CYP3A4 inhibitor	No	No
Excretion	Total Clearance (log ml/min/kg)	-0.899	-0.904
	Renal OCT2 substrate	Yes	Yes
Toxicity	AMES toxicity	Yes	Yes
	Max. tolerated dose (human) (log mg/kg/day)	0.541	-0.541
	hERG I inhibitor	No	No
	hERG II inhibitor	No	No
	Oral Rat Acute Toxicity (LD50) (mol/kg)	3.358	3.361
	Oral Rat Chronic Toxicity (LOAEL) (log mg/kg_bw/day)	2.115	2.115
	Hepatotoxicity	Yes	Yes
	Skin Sensation	Yes	Yes
	T. Pyriformis toxicity(log ug/L)	0.781	0.785
	Minnow toxicity(log Mm)	-5.207	-5.207

Table S6. Cheminformatics properties of the Ni(II) coordination complexes [Ni(L)]$_2$(**1**) and [Ni(L)]$_n$(**2**).

Model Name	Predicted Value	
	[Ni(L)]$_2$(**1**)	[Ni(L)]$_n$(**2**)
Molecular Formula	$C_{48}H_{36}Ni_2N_4O_4$	$C_{72}H_{54}N_6Ni_3O_6$
Molecular Weight (g/mol)	850.21	1275.34
GPCR ligand	-1.93	-3.27
Ion channel modulator	-3.01	-2.05
Kinase inhibitor	-2.67	-4.29
Nuclear receptor ligand	-2.79	-1.58
Protease inhibitor	-1.41	-1.57
Enzyme inhibitor	-2.38	-3.36
miLogP	-5.48	-7.21
TPSA	48.96	58.63
natoms	58	87
nON	8	8
nOHNH	0	0
nviolations	1	1
nrotb	1	1
volume	702.21	869.54
LogP	4.712	4.813
Rotatable Bonds	4	4
Acceptors	4	6
Donors	0	0
Surface area	86.36	129.54